Chemical Engineering Faculty Publications   Chemical Engineering

2023

Development of a porous layer-by-layer microsphere with branched aliphatic hydrocarbon porogens

Farah Shahjin

Milankumar Patel

Mahmudul Hasan

Jacob D. Cohen

Farhana Islam

See next page for additional authors

Authors

Farah Shahjin, Milankumar Patel, Mahmudul Hasan, Jacob D. Cohen, Farhana Islam, Md Ashaduzzaman, Mohammad Ullah Nayan, Mahadevan Subramaniam, You Zhou, Irene Andreu, Howard E. Gendelman, and Bhavesh D. Kevadiya

ELSEVIER

Journal logo

Original Article

Development of a porous layer-by-layer microsphere with branched aliphatic hydrocarbon porogens

Farah Shahjin PhD [a], Milankumar Patel MS [a], Mahmudul Hasan MPharm [b], Jacob D. Cohen BS [a], Farhana Islam BPharm [c], Md Ashaduzzaman BSc [d], Mohammad Ullah Nayan BPharm [a], Mahadevan Subramaniam PhD [d], You Zhou PhD [e], Irene Andreu PhD [f], Howard E. Gendelman MD [a], *, Bhavesh D. Kevadiya PhD [a]

[a] Department of Pharmacology and Experimental Neuroscience, University of Nebraska Medical Center, Omaha, NE, USA

[b] Department of Pharmaceutical Sciences, University of Nebraska Medical Center, Omaha, NE, USA

[c] Department of Biochemistry and Molecular Biology, University of Nebraska Medical Center, Omaha, NE, USA

[d] Computer Science, University of Nebraska-Omaha, Omaha, NE, USA

[e] Center for Biotechnology, University of Nebraska-Lincoln, Lincoln, NE, USA

[f] Department of Chemical Engineering, University of Rhode Island, Kingston, RI, USA

ARTICLE INFO

ABSTRACT

Porous polymer microspheres are employed in biotherapeutics, tissue engineering, and regenerative medicine. Porosity dictates cargo carriage and release that are aligned with the polymer physicochemical properties. These include material tuning, biodegradation, and cargo encapsulation. How uniformity of pore size affects therapeutic delivery remains an area of active investigation. Herein, we characterize six branched aliphatic hydrocarbon-based porogen(s) produced to create pores in single and multilayered microspheres. The porogens are composed of biocompatible polycaprolactone, poly(lactic-co-glycolic acid), and polylactic acid polymers within porous multilayered microspheres. These serve as controlled effective drug and vaccine delivery platforms.

© 2021

Introduction

Polymer microspheres (MS) facilitate delivery of drugs and vaccines.[1–4] Microfluidics and membrane-microchannel research have served to optimize MS synthesis. MS suspensions, dispersions, precipitations, and polymerizations all serving to improve drug, vaccine, and regenerative medicine cargo delivery.[5–17] For each of the polymer structure and porosity affect delivery as porosity and scaffold interconnectivity. These confer spatial, physical, and functional control in cell and tissue distribution, support, growth, and nutrient circulation for improved therapeutic outcomes and immune responses.[18] The macro- and micropores improve surface area facilitating MS delivery of nutrients, drugs, nucleic acids, and proteins. For biotherapeutic application, porosity affects surface area and in turn MS density leads to improved drug absorption and adsorption.[19,20] The surface topography can also affect cargo release which are linked to pore diffusion capacities.[12,21] Thus, the means to affect pore size are associated with how MS can facilitate cargo delivery.[22] However, control of such pore sizes and their interconnectivity remains challenging.[23] The importance of the type and quantity of the porogen used as well as how it influences polymer-pore morphology, surface area, volume, size distribution, rigidity, and mechanical stability is of pivotal importance as they all affect payload loading and distribution.[22,24] Based on such needs, research on porogens has focused on density, partition, polarity, and solubility as each and all, affect the MS physicochemical properties.[24]

Single polymer MS-based drug delivery systems underlie several research advances in nanomedicines.[1,25] In particular, MS containing

porous core-shells,[26–28] 'Janus' structures,[29] and multilayered structures[30–32] have served to improve cargo delivery and release while minimizing toxicities. Core-shell MS, in particular, allows the loading of multiple drugs with an order, timing, and dose release control.[33] This is based on stimuli-sensitive or pulsatile release of the payload, which is distinct amongst its layers.[27,34–36] Each and all provide a unique means for cargo administration while facilitating payload stability.[37] Herein, we provide a unique set of porogens that are designed to generate uniform pores, within single or multilayered biodegradable polymers. The porogens were characterized using solid-state characterization, demonstrating the ability to construct uniformly porous MS. We have also demonstrated the production of unique layer-by-layer (LBL) MS in a single-step process that optimizes timing and mixing of a specific biopolymer blend (Fig. 1) as demonstrated by structural and stability, biodegradation, and profiled release which serve to facilitate a novel drug delivery system. Taken together, the ability to alter MS porosity makes the study of broad interest as it influences a wide range of multilayered delivery systems.

Materials and methods

Reagents

All reagents were purchased from Sigma Aldrich, St. Louis, MO, USA, unless otherwise stated. The porogens used in this study include 2-methylpentane (2-MP) [Cat#M65807], 3-methylpentane (3-MP) [Cat#M66005], 2-methylhexane (2-MH) [Cat#M49704], 3-methylhexane (3-MH) [Cat#M49801], 2,3-dimethylbutane (2,3-DMB) [Cat#D151602], and 2,4-dimethylpentane (2,4-DMP) [Cat#D173401]. The polymers used include Polycaprolactone (PCL) – molecular weight ~ 40 k [Cat#19561, Polysciences, Inc., Warrington, PA, USA. [Cat#440744] and ~80k [Cat#440744], Poly(lactic-co-glycolic acid) (PLGA) 75:25 [Cat#P1941] and PLGA 50:50 [Cat#1001012896, Corbion, Gorinchem, Netherlands], Polylactic acid (PLLA) – PLLA-1 [Cat#765112], PLLA-2 [Cat#16585-10, Polysciences, Inc., Warrington, PA, USA], and PLLA-3 [Cat#1824013]. Other reagents include dichloromethane (DCM) [Cat#270997], acetone [Cat#A949-4,], polyvinyl alcohol (PVA, average 30,000–70,000 molecular weight) [Cat#P8136], Phosphate buffer pH 7.2 [Cat#P3288], Tween-80 [Cat#P1754], and Rhodamine B dye [Cat#283924] were from Thermo Fisher Scientific International Inc., Waltham, MA, USA.

Production of porous-single or multilayered polymer MS

MS were prepared by conventional solvent evaporation method.[4] PCL or PLGA or PLLA-2 (200 mg) was dissolved in 2 mL of DCM and vortexed to prepare the organic phase. Defined types and amounts of porogens (Table S1) were mixed and vortexed. The organic phase was added dropwise to the aqueous phase, consisting of 1 % (w/v) polyvinyl alcohol (200–300 mL) in a 600 mL capacity glass beaker (8.2 cm diameter), while constantly being stirred at 1000 rpm. An overhead stirrer (Cat#3593001, IKA, Wilmington, NC, USA) was used with a pitched blade propeller (Cat#14-500-363, Fisherbrand, Denver, CO, USA). The solution was left stirring overnight for organic solvent evaporation and polymer phase inversion. The porous MS were collected by filtration of aqueous phase using Whatman filter paper. Milli-Q water washes (~500 mL) were done to remove PVA and MS. These were lyophilized to obtain powder form for further characterizations. For layer-by-layer MS (LBL MS) production, the abovementioned solvent evaporation was used. Here the organic phase was prepared by com-
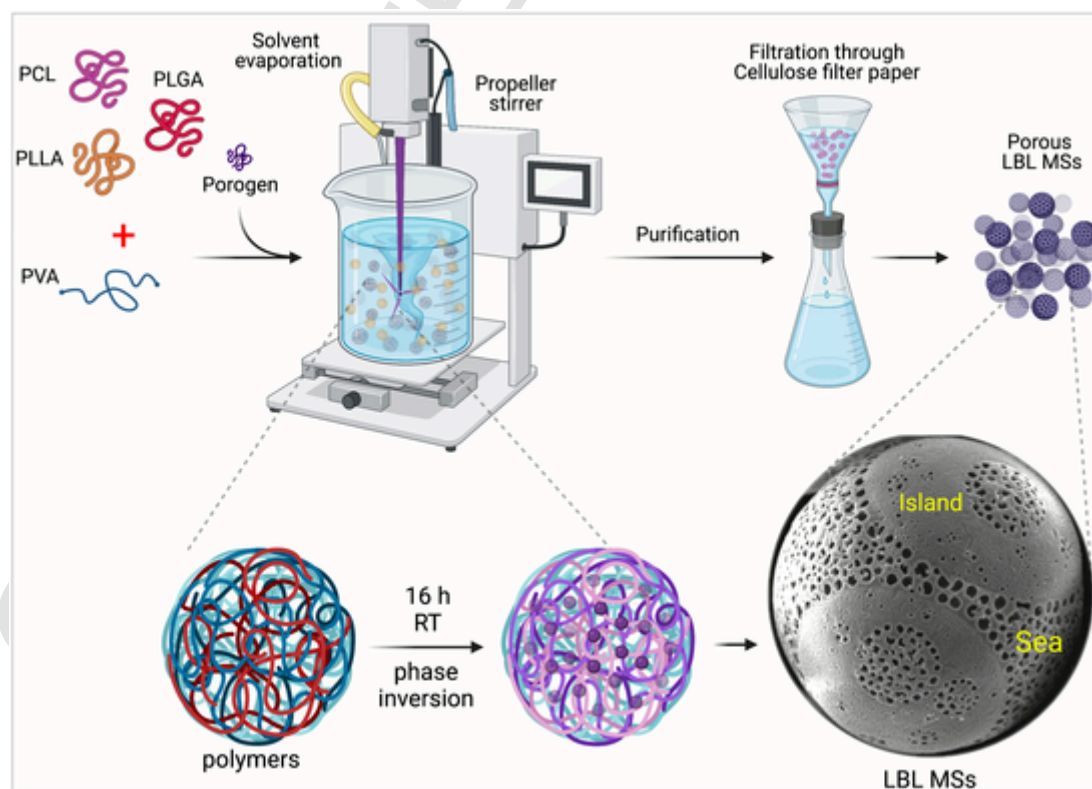

Fig. 1. Scheme of the porous LBL MS production. Single emulsion solvent evaporation technique employed the addition of the organic phase (polymer blend and porogens) to the aqueous phase (1 % PVA), stirred overnight at high speed at room temperature (RT). Organic phase evaporation allowed for the phase inversion of the polymers, while the porogens remained entrapped within polymer matrix. Leaching of porogens from polymer matrix left behind uniform pores with unique designing patterns, giving the MS an 'island-sea' external topography. The particles were purified by filtration and stored as lyophilized powder for further characterizations.

pletely dissolving PCL (100 mg), PLGA 75:25 (100 mg), and PLLA-1 (50 mg) in 1 mL of DCM prior to addition of the porogen (100 μL of 2-methylpentane) to the aqueous phase. The organic phase must be added to the aqueous phase while being stirred at 1000 rpm.

Scanning electron microscopy and image analyses

Lyophilized MS were collected on conductive adhesive carbon tape and attached to aluminum stubs. Particles were sputter-coated with 50 nm gold-palladium using Hummer VI Sputter Coater (Anatech, CA, USA); used at 10 mA for 5 min. They were imaged at 5–25 kV on an FEI Quanta 200 (FEI Company, OR, USA), operating in high vacuum mode. Based on SEM images, particle size distribution and porosity (pore size and density) measurements were performed in Google Colab using python libraries (cv2, imutils, skimage, scipy, matplotlib). For Google Colab analysis of particle size, electron microscopic images with at least twenty clearly visible MS were selected from the image pool of each polymer-porogen combination. For pore size distribution, a representative high magnification image (with planar surface of a MS) was selected from each polymer-porogen combination. Selected images were pre-processed by image filtering, segmentation, and binarization.[38] Gaussian blur filtering was used for the noise removal of the image. A mean shift filtering algorithm was applied to the images to shift the datapoint towards the centroids. Image thresholding techniques, which included Otsu's method, binary and binary-inverted methods were utilized for the segmentation of the image to create a binarized image.[39,40] Euclidean distances are measured for each foreground to the background pixels. Local maximums were calculated from each of the foreground images with different nearest neighbor images. The watershed algorithm was applied to separate the overlapping MS in the image.[41] From the output masks of the watershed algorithm, contours were detected. The largest contour for each mask was extracted as an individual particle or pore object. As most of the MS and pores were spherical, the enclosing circle boundary was calculated for each object. Enclosing circles, within a given radius range, were selected for the desired MS or pore objects. The red circled objects were drawn on top of binarized images as a task output. Image scales were detected from the lower right part of each image. Then, diameters of the detected circular objects were calculated as a second output of the task. For the pore distribution, subsequent analyses were done, (i) total surface area of the analyzed region of interest (ROI) (height*width), number of pores, and area covered by the pores. The summation of the areas of all pores in the ROI were calculated, and (ii) pore density (number of pores/surface area) and percentage of area covered by pores. Finally, the statistics from the result table were plotted using GraphPad Prism 9.2 (GraphPad Software, San Diego, CA, USA).

For cross-sectioning of the LBL MS (Fig. S1), we designed sectioning method in-house, by trial and error and this method has not been reported anywhere. The MS were immobilized in a gel matrix (commercial beauty product, Hemp+ facemask by My Beauty Spot, Amazon, USA) in a suitable mold (e.g., ultracentrifuge tubes, that can be cut by the blade). The MS-gel matrix was frozen at -80 °C for 10 min and 5–10 μm sections were obtained using Leica CM1850 (Leica Biosystems Inc., IL, USA) set at -20 °C. The slices were collected in warm water to wash off the water-soluble gel matrix and centrifuged at 5000 rpm to pellet the MS sections. Also, this product has readily water-soluble ingredients, allowing repeated quick washes of the MS with water at 37 °C. The choice of the gel matrix considered two criteria – (i) ability to freeze at -20 °C to -80 °C to immobilize the MS and allow microtome sectioning. The proprietary commercial product solidifies at -80 °C in a short time, without compromising the entrapped MS; (ii) dissolves readily in water at room temperature or 37 °C for matrix removal leaving behind free cut sections with no distortions. For acetone dissolution, acetone (500 μL) was added to MS of either PCL 40 k, PLGA 75:25, PLLA-1 or LBL MS (100 mg) for 1 h. MS were centrifuged to remove supernatant. The sectioned MS were lyophilized into powder form for SEM image analysis.

Spectroscopic characterizations of LBL MS

For Raman confocal microscopy, selected LBL MS were sectioned by freezing a droplet of MS suspension in water using liquid nitrogen and sectioning the frozen droplet using a clean new steel razor blade. The low temperature reduces plastic deformation during sectioning. The MS were air dried on a glass slide and imaged on a WITec alpha 300R confocal Raman microscope equipped with a 532 nm laser and a 600 g/mm grating. Raman hyperspectral maps were obtained using a 50× objective (Zeiss Epiplan-NEOFLUAR NA = 0.8), a laser power of 5 mW and 10 accumulations of 1 s per data point, with a distance of 20 μm between data points. The hyperspectral maps were processed by True-Component™ on the WITec Project Five software to find the two main components of the mapped region. Single spectra of pure PCL 40 k, PLGA 75:25 and PLLA-1 were acquired on the same system and compared to the components found on the MS. Fourier Transform Infrared spectroscopy were recorded on a Perkin-Elmer-spectrum attenuated total reflectance (ATR)-FTIR equipped with a UATR-accessary (Perkin-Elmer, Inc., Waltham, MA, USA).[42] The spectra were recorded for single polymer MS and LBL MS. The scanning range was 400–4000 cm^{-1}, and the resolution was 2 cm^{-1}.

For X-ray microscopy (XRM), dry powder of LBL MS was run on a Zeiss Xradia Versa 610 X-ray microscope operated at 80 kV, 10 kW, 4× optical magnification at 1.56 μm voxel size with 1 s exposure time and 1601 projections, to achieve a 3D reconstruction of the MS. The tomography(s) were analyzed with Dragonfly Pro (Object Research Systems, version 2021.1.0.977) to calculate MS size. The acquired tomograms were filtered using a Gaussian blur to remove low frequency noise and segmented into particles and void space using the Dragonfly Pro machine learning module. The segmented particles were separated using watersheds and their minimum Feret diameters were calculated to obtain the size distribution. Fibrous debris or particles not completely captured or separated in the tomogram were not considered in the size distribution.

Surface chemistry and structural analysis of LBL MS

X-ray photoelectron spectroscopy measurements were carried out using monochromatic Al K$_a$ X-ray with an energy of 1486.6 eV by the K-alpha XPS system (ThermoFisher Scientific, Waltham, MA, USA).[43] The spectra were generated using GraphPad Prism 9.2 software. The crystalline nature of the microspheres was investigated by X-ray powder diffraction (XRD), using Rigaku SmartLab Diffractometer (Rigaku Corporation, Tokyo, Japan), operated with Cu Kα radiation at 40 kV and 30 mA.[43] A length limiting slit of 10 mm, a divergence slit of 1/2° and a 5° Soller slit were used on the incident beam path and the data was collected by q/2q scans using a D/tex Ultra 250 1D strip detector with 20 mm receiving slits and a 5-degree Soller slit. A Ni foil was used to suppress Kb intensity. The MS were spread in a 20 × 20 mm, 0.2 mm deep pocket of the sample holder and the surface was leveled. The data was collected from 15 to 35°, continuously scanning q/2q scan at 0.6 s/step with a step size of 0.01. The spectra were generated using Origin-Pro 2021 software.

Thermal analysis of LBL MS

For the differential scanning calorimetry (DSC) analysis, samples and reference were heated in an inert nitrogen atmosphere with a nitrogen flow rate of 20 mL/min that was subjected to a heating cycle between 25 and 500 °C with a heating rate of 10 °C/min in NETZSCH DSC 204 F1 Phoenix (NETZSCH, Waldkraiburg, Bayern, Germany). For the thermogravimetric analysis (TGA), samples were measured using NET-

ZSCH TGA 209 F1 Libra system (NETZSCH, Waldkraiburg, Bayern, Germany). TGA thermograms were obtained between 20 and 700 °C with a constant heating rate of 10 °C /min under nitrogen gas (flow rate of 20 mL/min). The data was analyzed using NETZSCH Proteus-thermal analysis-Version 6.1.0 software. The spectra were generated using OriginPro 2021 software. To study the effect of temperature on the MS external morphology, LBL MS (200 mg) were stored at room temperature, 4 °C, -20 °C and -80 °C. At different time points, samples were collected for SEM. For *in vitro* biodegradation simulation, the LBL MS (100 mg) were immersed in buffered cell culture media (supplemented DMEM media), at pH 5.5 and 7.5. Sink media was changed every 7 days, and aliquots of MS were washed, freeze-dried, and prepared for SEM. To study the effect of temperature on the MS morphological stability, LBL MS (200 mg) were stored at room temperature, 4 °C, -20 °C and -80 °C. Samples were collected for SEM at different time points.

Confocal laser scanning microscopy

The samples were visualized in a Nikon A1R+ confocal laser scanning system on a Nikon Ti2 inverted microscope (Nikon Instruments Inc., Melville, NY, USA) using the 10× objective. Raw polymers, polymer MS, and LBL MS were all excited with a single laser line (401, 488, 560, or 639 nm) and the emission spectra (10 nm step separation within a range of 404–660 nm) for each excitation of each sample was collected under same acquisition settings (such as laser power, gain and intensity constant) using the Nikon NIS-Element program, respectively. Spectral images acquired were analyzed using NIH ImageJ-Fiji program and mean fluorescence intensity (MFI) was measured for the whole panel for each excitation and emission wavelength, respectively. The collected MFI values were plotted using GraphPad Prism for neat polymers, individual polymer MS, and LBL MS. Emission in the excitation wavelength was excluded from the graph.

Biodegradation and release profiling

For *in vitro* biodegradation simulation, the LBL MS (100 mg) were immersed in buffered cell culture media (supplemented DMEM media), at pH 5.5 and 7.5. Sink media was changed every 7 days, and aliquots of MS were washed, and freeze-dried for SEM analyses. *In vitro* release studies were performed to measure Rhodamine B (RhB) release from LBL MS using a USP dissolution testing system (Sotax AT7 Smart Semi-Automated Dissolution Tester, SOTAX Corp, Westborough, MA, USA). RhB dye release experiments used the dialysis bag technique[44] (dialysis tubing cellulose membrane, MWCO 14 kD, Millipore Sigma, Milwaukee, WI, USA) in phosphate buffer (PB; Millipore Sigma, Milwaukee, WI, USA) with 1 % (v/v) Tween-80, one set at pH 7.2 and another at pH 5.5. Sixty milligrams of porous or non-porous LBL MS with RhB payload were placed in dialysis bags containing 5 mL of the respective release medium. The bags in mesh stainless steel baskets were immersed in the Tester well containing 300 mL of release medium at a temperature of 37 ± 0.5 °C and set to 150 rpm. Samples were withdrawn at regular time intervals and the same volume was replaced with fresh release medium. Samples were analyzed for RhB content by Spectrofluorometer (RF6000, Shimadzu, Columbia, MD, USA) at λ_{ex} 560 and λ_{em} 585 nm, and if necessary were further diluted with PB at the corresponding pH. This analysis was performed with triplicate samples per pH, and the spectrophotometer reading per sample was done in triplicate. The average values were used for data analyses (standard curve-based concentration measurements) by GraphPad Prism 9.2. The release profiles of RhB from LBL-RhB MS were each fitted with 2-step release kinetics mathematical model.

Results
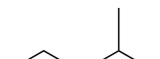
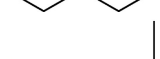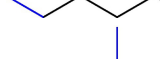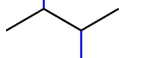### Characterization of a single or multipolymer 'porous' MS

Porogen polymers

Single polymer microspheres were prepared by single emulsion solvent evaporation, using PCL, PLGA 75:25, and PLLA-2 polymers, to evaluate the pore forming capacities of six chemicals, which were branched aliphatic hydrocarbons. These included 2-methylpentane (2-MP), 3-methylpentane (3-MP), 2-methylhexane (2-MH), 3-methylhexane (3-MH), 2,3-dimethylbutane (2,3-DMB), and 2,4-dimethylpentane (2,4-DMP) (Table 1). SEM analysis was used to assess the pore forming effects on the polymer MS. Particle size and pore size distributions were analyzed from representative SEM images. Image analysis was completed in Google Colab using python libraries, where the contours (yellow), of either the pore (Fig. S2) or MS (Fig. S3, A-C), were analyzed on the output masks with the watershed algorithm. The pores generated in the MS were spherical in shape with varying depth (Fig. 2A). The pores generated in PCL by all six porogens were larger, as depicted by >60 % porosity (Fig. 2B), which in turn resulted in lower number of pores per particle, particularly for MS prepared with 2-MH, as depicted by the pore density (Fig. 2C). In case of PLGA MS, the pores formed on PLGA were superficial with about ~35–50 % porosity (Fig. 2B) with the exception of 2-MP, which had low pore density (Fig. 2C). PLLA-2 prepared with the six porogens individually had comparable % porosity (≥ 50 %) and density (≥ 0.02).

SEM images were then analyzed for particle size distributions (Fig. S3A-C). The MS generated were spherical in shape, with heterogeneous size distributions (Fig. S3D). Mean diameters of the PCL MS were 80.2 ($S_E \pm 2.9$), 104.2 ($S_E \pm 4.5$), 149.6 ($S_E \pm 5.8$), 85.7 ($S_E \pm 2.8$), 90.4 ($S_E \pm 2.5$), 92.6 ($S_E \pm 2.8$) µm, for PLGA were 63.6 ($S_E \pm 4.6$), 77.1 ($S_E \pm 2.6$), 83.8 ($S_E \pm 5.8$), 79.3 ($S_E \pm 2.5$), 51.0 (SEM ± 4.8), 88.2 ($S_E \pm 3.2$) µm, and for PLLA-2 were 92.4 ($S_E \pm 3.9$), 90.8 ($S_E \pm 3.2$), 64.7 ($S_E \pm 4.1$), 65.3 ($S_E \pm 4.6$), 95.3 ($S_E \pm 3.5$), and 61.0 ($S_E \pm 3.1$) µm. Mean diameter was high for porous PCL MS made with 2-MH, showing larger particle sizes (mean diameter = 150 µm) than the other PCL MS (mean diameter ranging from 80 to 105 µm) made with the different porogens.

Table 1
Physicochemical properties of the branched, aliphatic hydrocarbons 'porogen'.

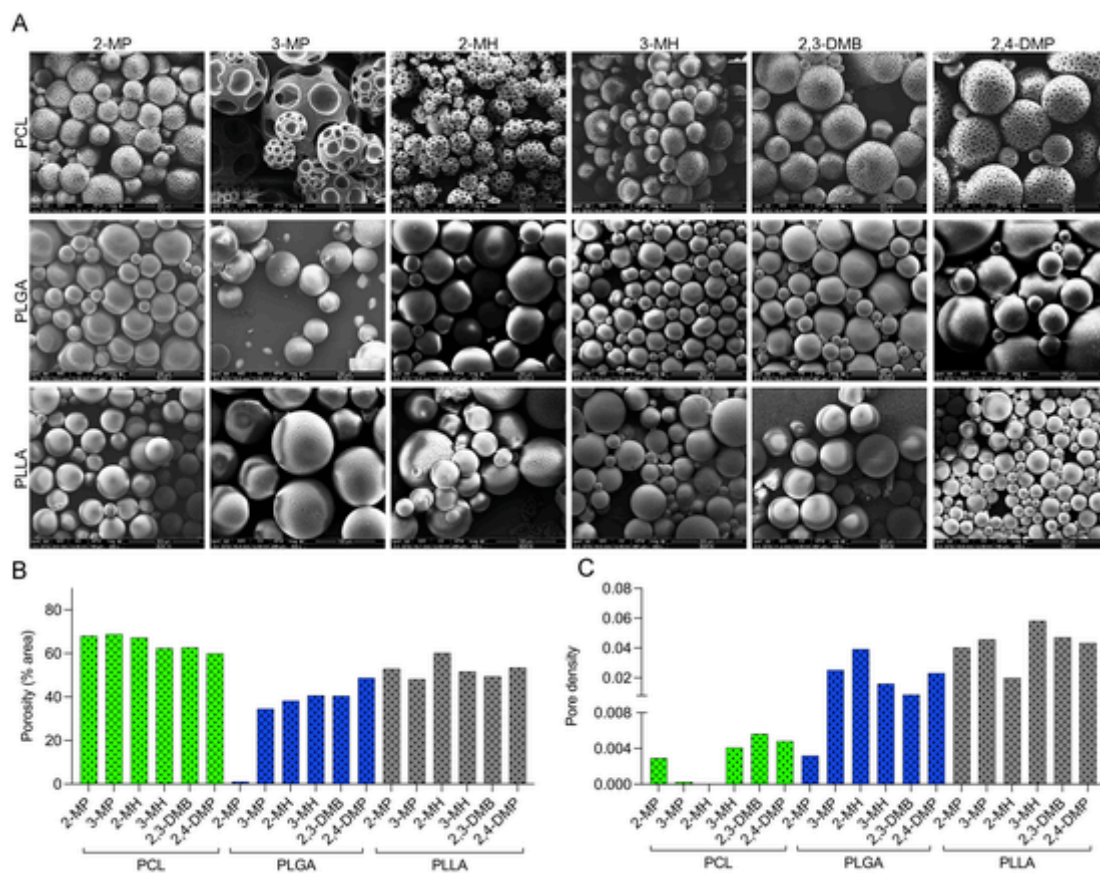| Porogen chemical name	Porogen chemical structure	Boiling point (°C)	Density (kg/m³)	Miscibility with DCM
2-methylpentane (2-MP)		60 °C	653	Miscible
3-methylpentane (3-MP)		63 °C	670	Miscible
2-methylhexane (2-MH)		92 °C	670	Miscible
3-methylhexane (3-MH)		90 °C	687	Miscible
2,3-dimethylbutane (2,3-DMB)		58 °C	660	Miscible
2,4-dimethylpentane (2,4-DMP)		80 °C	697	Miscible

Fig. 2. Effects of the branched aliphatic hydrocarbon porogens on porosity of different polymers. (A) SEM images show the MS made of PCL, PLGA, or PLLA with the six different aliphatic hydrocarbon-based porogens (2-MP, 3-MP, 2-MH, 3-MH, 2,3-DMB, and 2,4-DMP). Scale bar: depicted at the lower bar of respective images, (B) Porosity (pore size and density) measurements were performed in Google Colab using python libraries (cv2, imutils, skimage, scipy, matplotlib). Porosity (% area) measurements were done from the representative SEM images by calculating the total area covered by the pores (summation of the areas of all pores in the image), and (C) Pore density measurements from representative SEM images, by dividing the number of pores in the analyzed area by the surface area of the analyzed region (height*width).

Porogen pattern, size, and porosity

The porogen properties of solvents are related to its quantity and miscibility.[45,46] Therefore, the effects of varying the ratio of porogens to polymers was also investigated. Based on surface observations by SEM, an increase in the quantity of porogen used, from 200 μL to 400 μL of 2-MP, increased the pore size on the MS, with obvious changes in surface smoothness and visible depth of the pores (Fig. 3). We also observed that the changes in pore patterns when changes were made in molecular weights (in case of PCL and PLLA) and composition (in case of PLGA 75:25 and 50:50) of the polymers. MS prepared with 400 μL 2-MP exhibited visibly deeper pores, for PCL ~40 k and ~ 80 k, and PLLA-1 and 3. There were no visible changes on PLGA 75:25. Overall, changes in porogens can change the porosity of MS. Additionally, the porogen effects were also affected by the molecular weights and composition of the same polymer. These observations mandate optimization in the MS production process considering different porogen-polymer combinations.

Interestingly, a change in porogen to polymer ratio affected the porosity and the MS morphology. The analysis of porous structure was prepared with PLGA 50:50 and distinct from PLGA 75:25-derived MS (Fig. 3). For PLGA MS prepared with 200 μL 2-MP, PLGA 75:25 had comparable porosity to PLGA 50:50, but a rough external surface. When 400 μL porogen was used for PLGA MS, not only did the pore sizes change for PLGA 50:50, but also the particles assumed a hemispherical morphology. This is a stern departure from the spherical structure of all other generated particles. The pore sizes were visibly larger in PLGA 50:50 hemispheres than in PLGA 75:25 spheres when both received

equal quantities of porogen. Varied volumes of 2-MP (300 to 400 μL) were used to observe the exact threshold where the particles split in half (Fig. S4A). Other five porogens, in different quantities (200 and 400 μL) were also used to investigate porogen's effects on PLGA 50:50 polymer types and particle shape (Fig. S4B). It was observed that the effects of the different porogen effects varied when used with PLGA 50:50. Specifically, 3-MP, 3-MH, 2,3-DMB, and 2,4-DMP generated hemispheres instead of spherical particles when higher amounts of porogens were used. Only 2-MH did not seem to generate such hemispheres, yet instead produced fragile, hollow, and porous MS. Moreover, the uniformity of pores was dependent on quantity of porogens, again highlighting the importance of production process optimization.

Porous LBL MS

Biodegradable polymer MS are widely used in the development of controlled delivery systems because of their reduced side effects through extended dosing and targeting.[47,48] Multilayered MS have the potential to control drug delivery for pharmaceutical applications.[27,36,49] Considering the importance of developing a stable multilayered platform, a polymer blend of PCL, PLGA and PLLA was successfully produced into LBL MS, using single emulsion solvent evaporation technique.

To our knowledge, no multilayer MS production method had been demonstrated previously that allows porosity inclusion in multilayers. In that process, the 2-MP porogen demonstrated the ability to create pores across different polymer layers (Fig. 4). The external morphology and internal architecture of the LBL MS were determined using state-of-
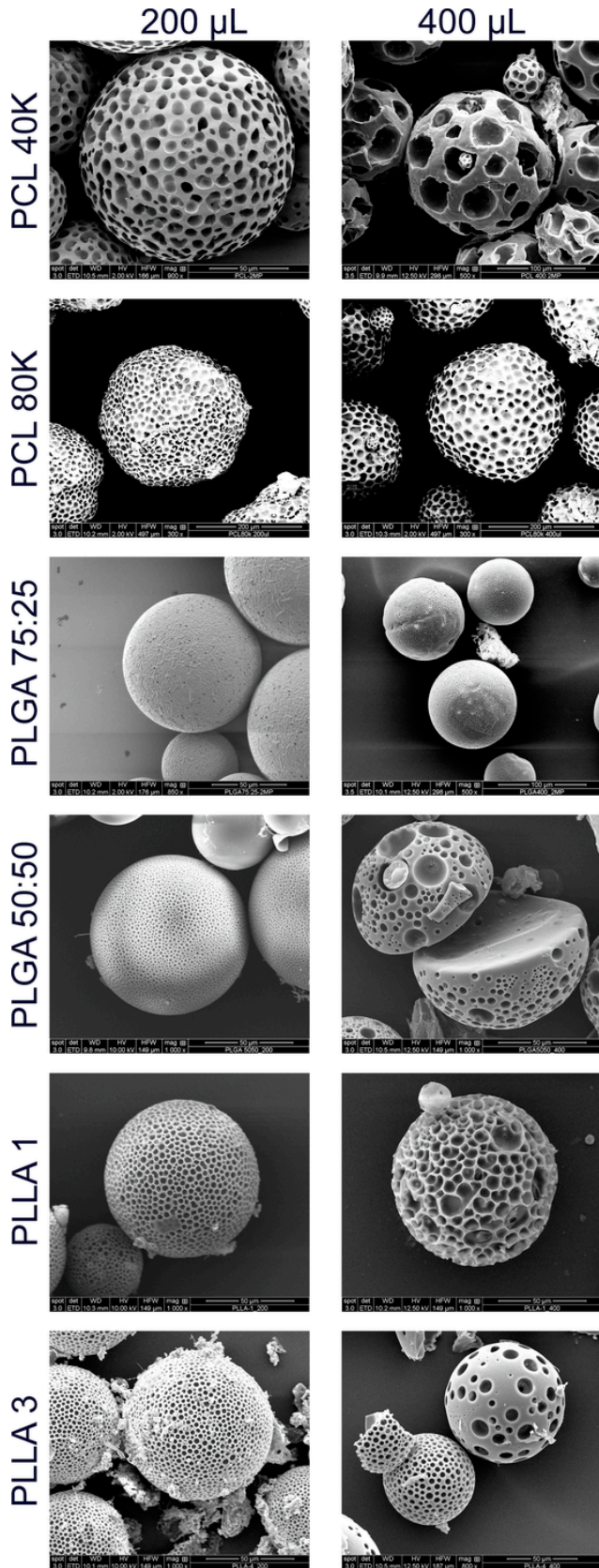
Fig. 3. Effects of porogen quantity on MS morphology. Polymers of different molecular weights/compositions were prepared by single emulsion solvent evaporation method, all in the same manner, with a low (200 μL) and high

(400 μL) amount of the porogen, 2-MP. Polymers used were PCL (molecular weights ~40 k and ~ 80 k), PLGA – 75:25 and 50:50 by PLA: PGA content, and PLLA-1 (Mn 10,000) and 3 (Mn 17,000). SEM images show the differences in pore sizes and depth, as well as particle shape (in the case of PLGA 50:50 only). Scale bar: depicted at the lower bar of respective images.

art microscopic techniques. SEM images showed the typical external, smooth morphology of the non-porous LBL MS (Fig. 4A, left). The cross-section of the non-porous MS illustrates the distinct layers of the different polymers. For the porous MS (Fig. 4A, middle), the external surface consisted of pores, with numerous regular spherical inclusions (like 'pellets') in a matrix of polymer. The patches were also porous and isolated, with definite borders separating them from the matrix, metaphorically depicting an 'island-sea' topography. The cross-section of the porous LBL MS (Fig. 4A, right), showed the definite double layered architecture with pores generated in both the layers. Zoomed images of the double-layer revealed that the external layer incorporated numerous regular, porous spherical inclusions. The SEM images showed that the polymers form a distinct double-layered structure, with uniform distribution of pores in every layer due to porogen, 2-MP.

The X-ray microscopy (XRM) data for LBL MS was consistent with the observations through SEM. MicroCT 3D reconstruction of the LBL MS (Fig. 4B) confirmed that the MS were spherical and had a core-shell morphology and had a solid core and a porous shell. The histogram of the 3D particles' diameters (Fig. 4C) was obtained by XRM (n = 84), and the data showed that the MS diameters ranged from 135 to 380 μm, with an average particle size of 240 ± 52 μm corroborating the SEM data.

To identify the internal polymer composition of the LBL MS, the cross-sectioned MS were subjected to acetone dissolution test. Acetone is reported to dissolve PLGA more readily than PLLA and PCL.[50] Upon acetone treatment, the shell retained the intact spherical structure (Fig. 4D, left), the spherical patches remained undissolved by acetone. Such results combined with the fact that the pellets in the shell were distinct from the shell matrix, it indicated that the pellets were likely to be composed of PLLA while the majority of the shell was composed of PCL. The sections had a hollow shell structure, demonstrating the dissolution of the PLGA core (Fig. 4D, right). These results demonstrate that the LBL MS were composed of a PCL shell and PLGA core, with surface pellets composed of PLLA.

Spectroscopic characterizations

To further verify the composition of the multilayers of the MS, Raman microscopy and spectral analysis were performed for LBL MS. Combination of Raman optical microscopy, demonstrating the spatial resolution, and hyperspectral mapping (Fig. 5), corroborated the SEM observations, showing the distinct polymer layers into a core-shell architecture. The combination of the confocal Raman microscopy data (Fig. 5A) and the Raman spectroscopy data (Fig. 5B) allowed for visualization of the MS PCL shell (cyan) and the MS PLGA core (magenta) corresponding to PCL and PLGA respectively. Characteristic peaks (Fig. 5C-D) belonging to PCL-[2916 cm^{-1}, 2871 cm^{-1}, 1729 cm^{-1}, 1447 cm^{-1}, 1307 cm^{-1}, 1287 cm^{-1}, 1113 cm^{-1} and 1070 cm^{-1}], characteristic peaks belonging to PLGA 75:25 - [3003 cm^{-1}, 2949 cm^{-1}, 2888 cm^{-1}, 1774 cm^{-1}, 1461 cm^{-1}, and 870 cm^{-1}], and characteristic peaks belonging to PLLA - [3002 cm^{-1}, 2949 cm^{-1}, 1772 cm^{-1}, and 878 cm^{-1}] could be identified in the spectra of the individual neat polymers. The characteristic peaks of the raw polymers were seen to overlap with the distinct peaks obtained from the blend made from PLGA/PLLA/PCL LBL MS. Characteristic peaks of PCL at 2916 cm^{-1}, 2871 cm^{-1}, 1729 cm^{-1}, 1447 cm^{-1}, 1307 cm^{-1}, 1287 cm^{-1}, 1113 cm^{-1} and 1070 cm^{-1}, can all be seen to overlap with the spectra of the LBL MS shell. Characteristic peaks of PLGA at 3003 cm^{-1}, 2949 cm^{-1}, 2888 cm^{-1}, 1774 cm^{-1}, 1461 cm^{-1}, and 870 cm^{-1} can be seen to overlap with the spectra of the LBL MS core. This confirmed that PCL was
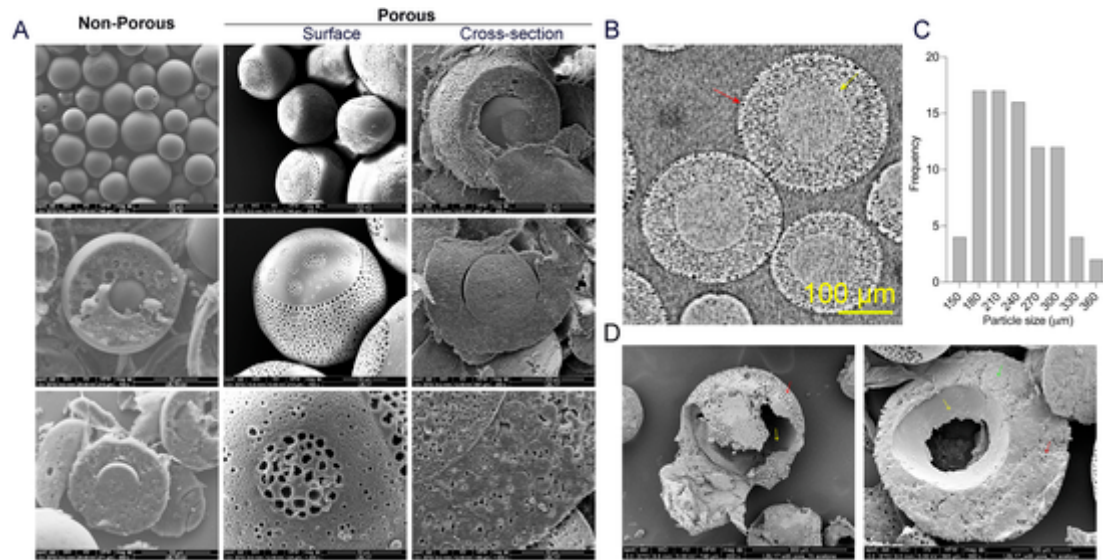
Fig. 4. Microscopic evaluation of LBL MS morphology, with or without pores. (A) SEM images show (left) external morphology and cross-section of non-porous LBL MS, (middle) external morphology of porous MS with 'island and sea' topography, and (right) cross-section of the porous LBL MS with distinct 'core-shell' layout. A zoom image of the cross-section shows the pores and polymer pellets in the shell layer. Scale bar: depicted at the lower bar of respective images. (B) Representative virtual cross section of a few LBL MS as measured by XRM, showing a distinct core (yellow arrow) and shell (red arrow) morphology. Scale bar: 100 μm, (C) Histogram of XRM based measurements of the 3D particle diameters (n = 84), showed that the MS diameters go between 135 and 380 mm, with an average particle size of 240 ± 52 mm, (D) LBL MS sections (10 μm) were subjected to acetone for 1 h for PLGA solubilization, then lyophilized and imaged by SEM to reveal (left) the intact, spherical shell architecture (red arrow) and the hollow internal space (yellow arrow), (right) the zoom image of a solubilized core (yellow arrow) and insolubilized shell (red arrow). The polymer pellets associated with the shell were insolubilized as well (green arrow). Scale bar: depicted at the lower bar of respective images. (For interpretation of the references to color in this figure legend, the reader is referred to the web version of this article.)
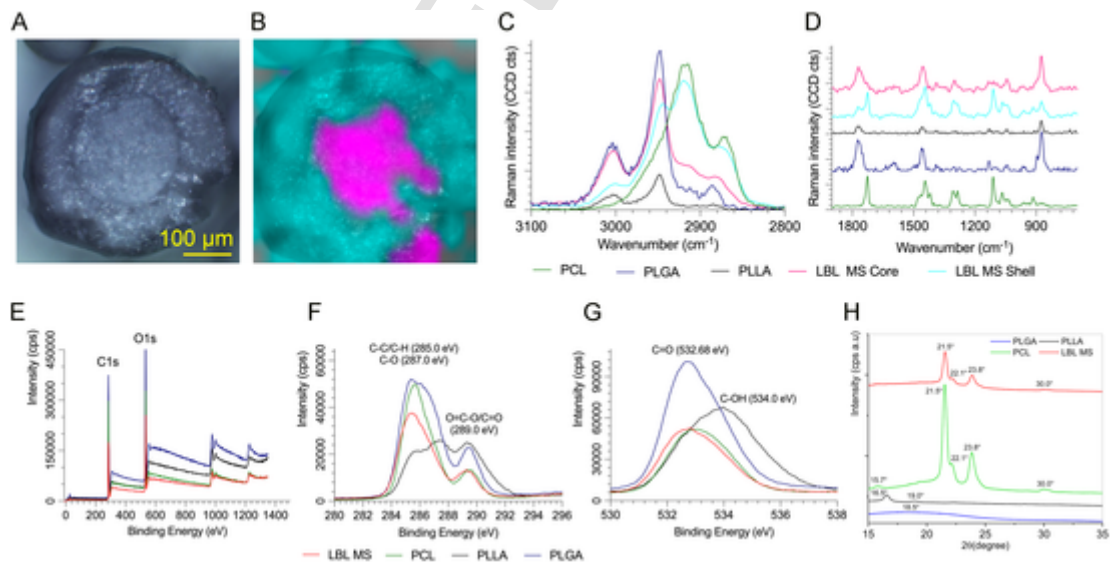

Fig. 5. Spectroscopic and microscopic characterization of LBL MS. (A) Brightfield microscopy image of a representative sectioned LBL MS, and (B) the overlaid spatial distribution of components found by Raman spectroscopy, showing the distinct polymer layers, with the core (magenta) and shell (cyan) components; (C-D) Comparison of the Raman spectra from the core (magenta) and shell (cyan) regions of the LBL MS and the individual polymers – PCL (green), PLGA (blue) and PLLA (black). XPS analysis of LBL MS compared with native polymers, showing (E) the C1s and O1s wide spectrum, (F) C1s and (G) O1s high-resolution spectra and characteristic functional group peaks for individual raw polymers and LBL MS, and (H) XRD analysis of LBL MS from bottom to top: XRD patterns of raw polymers (PLGA, PLLA, PCL) and LBL MS. (For interpretation of the references to color in this figure legend, the reader is referred to the web version of this article.)

the main component in the shell while PLGA was the main component in the LBL MS core. Characteristic peaks of PLLA at 3002 cm⁻¹, 2949 cm⁻¹, 1772 cm⁻¹, and 878 cm⁻¹ were all seen to overlap with the spectra of the shell and core, but not PCL. This indicates that PLLA was incorporated at both shell and core, suggesting that the patches on the shell matrix were possibly composed of PLLA. However, due to similarities in molecular structures of PLLA and PLGA, their Raman spectra were indistinguishable.

To corroborate the Raman spectral results, FTIR was used to verify the functional groups of the polymers existing in the samples (Fig. S5). In the case of neat PLGA 75:25, the IR peaks at 2990 and 2947 cm⁻¹ correspond to the C—H stretch of -CH₂, and the C—H stretch of —CH respectively, 1746 cm⁻¹ was assigned to the stretching vibration of the carbonyl group (C=O) of the ester bond, and 1083 cm⁻¹ was attributed to C—O stretching. In the case of raw PCL, typical bands at 2941 cm⁻¹ (asymmetrical CH₂ stretch), 2864 cm⁻¹ (symmetrical CH₂ stretch),

1045–1165 cm^{-1} (C—O stretch) were seen. Also, characteristic IR peaks were obtained at 1722 cm^{-1}, corresponding to the conjugated carbonyl group (C=O), and in the region of 1000 to 1500 cm^{-1}, corresponding to C—C, C—H and C—O groups. Similar to PLGA, PLLA also showed strong bands in the region 2995 and 2946 cm^{-1} for asymmetric and symmetric -C-H stretching, respectively. Also, bands at 1753 and 1080 cm^{-1} were seen due to the stretch of the C=O and C—O groups, respectively. There are also stretching bands due to asymmetric and symmetric C—O vibrations between 1300 and 1150 cm^{-1}. These spectra matched the expected individual polymer profiles from past literature for the individual polymers.[51–53] The absorption bands of the LBL MS overlapped with the individual polymer bands confirming the triple polymer composition of the LBL MS.

Shell composition was further confirmed by X-ray photoelectron spectroscopy (XPS), a surface element analysis technology, which provides quantitative and qualitative information of the elements on the LBL MS surface within 10 nm thickness.[54] All raw polymers, core and the shell structures were predominantly composed of the elements carbon (C) and oxygen (O) with binding energies 285 and 532 eV, as evidenced by the photoelectron lines in the wide scan spectrum (Fig. 5E). The high-resolution spectrum (Fig. 5F), corresponding to the C1s wide spectrum, depicted four types of carbon bonds: C—C/C—H (285 eV), C—O (287 eV), C=O (289 eV), and O—C=O (289 eV). The high-resolution spectrum (Fig. 5G) corresponding to the O1s wide spectrum, depicted two types of oxygen bonds: C=O (532.68 eV) and C—OH (534 eV). The decrease in intensity of the C1s and O1s peak for LBL MS was due to the three polymers' existence in a blend and in a spherical morphology instead of the neat polymeric state. All the XPS binding energies were in accordance to the previously published reports.[54] Overall, the superimposing spectral data showed that the surface composition of the LBL MS shell was of PCL.

The XPS data was further corroborated using X-Ray Diffraction (XRD) analyses. Two intense peaks in the XRD were obtained at diffraction angles of 2 θ; 21.5° and 23.8°, indicating that raw PCL and LBL MS were in its semi-crystalline form (Fig. 5H). On the other hand, raw PLGA and PLLA had no distinct peaks, indicating it remained in the amorphous form. In theory, XRD identifies crystalline materials within about 10 μm of the surface[55] and the MS we generated were much larger. Thus, the XRD curve only revealed the surface composition, which is predominantly PCL.

Thermal analyses of LBL MS

DSC thermograms of the neat polymer components and the LBL MS were generated to evaluate the thermal properties of the LBL MS. The melting peaks of neat PCL, PLGA and PLLA were observed at approximately 63.7, 82.5 and 173 °C, respectively. Similar melting peaks were seen for the LBL MS at 61.4 and 168 °C (Fig. 6A). The minor shift in the LBL MS peaks indicate PCL/PLLA/PLGA dispersion inside the LBL MS. After 300 °C, raw polymers and the LBL MS showed decomposition. More evidence of the LBL MS thermal properties was obtained from TGA thermograms (Fig. 6B) and differential thermal analysis (DTA) (Fig. 6C). As shown in Fig. 6B, the thermal decomposition temperature of PCL had initial and complete decomposition temperatures of ~380 and 420 °C (mass change = 97.69 %), respectively. PLLA and PLGA had lower initial and complete decomposition temperatures, down to 240 and 350 °C for PLLA (mass change = 94.85 %), and 270 and 360 °C for PLGA (mass change = 80.45 %). The weight decrement of PLGA is biphasic and the first loss between ~75-100 °C can be attributed to the water loss.

This result may be attributed to the decreased crystallinity of PLLA and PLGA compared to PCL and was consistent with the previously published literature.[56,57] The multi-phasic weight loss of LBL MS was seen between ~75 and 125 °C (mass change = 8.54 %) and ~230 to 400 °C, with maximum weight reductions in two phases - the first at temperature ~ 288 °C (mass change = 52.68 %) and second at ~350 °C (mass

change = 50.15 %). The shift in curve of LBL MS, showing degradation at lower temperatures than PCL, can be attributed to the added PLGA and PLLA.

Additionally, DTA analysis is an alternative thermoanalytical technique, important for the solid-state characterization of pharmaceutical materials[58] to determine loss on drying, phase transition temperatures, thermal stability, and whether or not water is bound or unbound. The DTA thermograms in Fig. 6c showed extreme weight reduction at 408 °C for PCL and at 314 °C for PLLA and PLGA. Again, the differential weight loss between ~75 and 100 °C for PLGA can be attributed to the water loss. The thermogram for LBL MS showed two distinct peaks, at 330 °C and 388 °C, corresponding to the decomposition peaks of the individual polymers. The shift further confirmed the presence of the three polymers in the MS. The overall shifted curve for LBL MS had a weight loss pattern as well as initial and complete decomposition temperatures reflective of all three polymers, proving the presence of PCL, PLGA and PLLA in the LBL MS as well as their stability at high temperatures.

Besides determining the analytical thermal stability of the MS, it is also important to identify the suitable long-term storage temperatures for these particles. Polymer MS have wide application in drug and peptide delivery. Once payload encapsulation has been achieved, up until its administration, the formulation is required to be stored at conditions that will prevent payload or polymer degradation. We performed additional visual inspection by SEM to investigate any changes in particle morphology when stored at temperatures 4 °C, −20 °C, −80 °C, or room temperature, which are ideally used for storage and handling of parenteral formulations. SEM images were taken at days 7, 28, 42 and 130, (Fig. 6D). No visible particle degradation or changes in porosity patterns were observed, ensuring that carrier particles were stable at any of the selected temperatures. In cases where antigenic payload is the intended payload, cooler storage temperatures are required, mandating the study of the LBL MS stability at different storage temperatures. We have subjected the LBL MS to the general storage temperatures suitable for peptide/protein-based cargo storage and have found that the formulation can be stored long term without any major changes in morphology and porosity.

Biodegradation

Controlled drug release from MS depends on the particle size, porosity, roughness, and composition of particles.[59–62] For instance, MS with porous and rough surfaces achieve faster release because of enhanced diffusion of the solvent through the pores.[12,21] An in vitro simulation of the LBL MS biodegradation was performed to study the particle degradation pattern at pH 5.5 ad 7.4. The pH were intended to reflect the in vivo ambience – injection site tissue pH of 7.4 or the intracellular endosomal acidic pH ranging from 4.5 to 5.5.[63] The time course (Fig. 7A) of the degradation of the porous LBL MS spanned six months at in vitro simulated neutral (tissue pH, extracellular or cytoplasmic pH) and acidic (endosomal and lysosomal pH) environments (Fig. 7A). SEM images show that the particles suspended at pH 7.2 showed visible surface erosion by week 3, as evidenced by the retracting shell surface and visible pellet protrusion from the eroding surface. Surface erosion resulted in the release of pellets of smaller MS (the shell 'islands') by week 5 and subsequent bulk degradation by week 24. Similar surface erosions were observed at acidic pH but at an earlier timepoint, i.e., starting near week 1. Understandably, the faster onset of degradation at pH 5.5 can likely be attributed to the autocatalysis of the polymers induced by the degrading polymer's acidic byproducts.[64] By week 24, most of the particles have disintegrated completely at both pH. Overall, the LBL MS demonstrated surface erosion with smaller 'pellet' MS release and eventual bulk degradation.

Release

Polymer-based micro-and nanoparticles are increasingly investigated for sustained release and targeted drug, peptide/protein, and
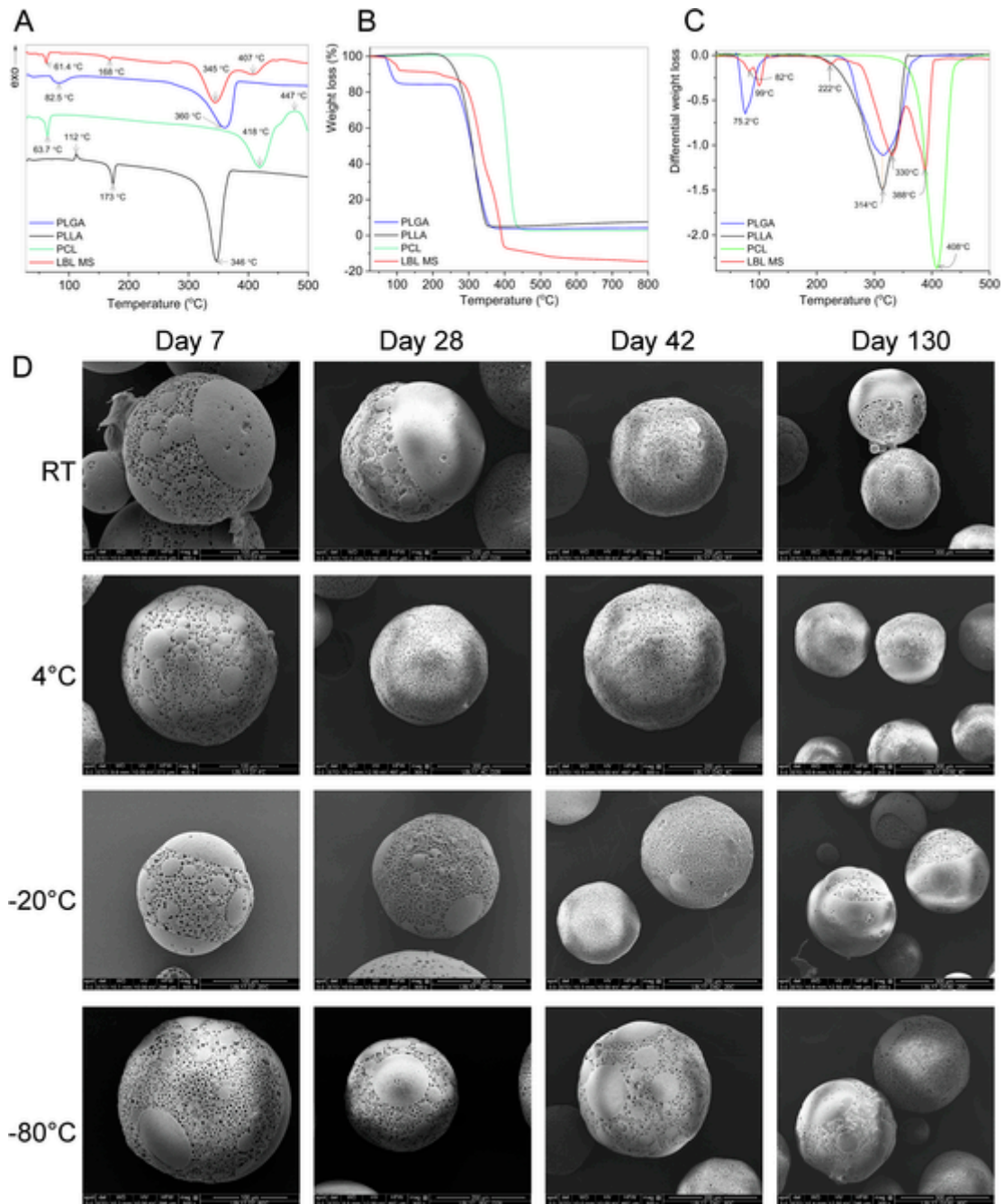
Fig. 6. Thermal analysis of LBL MS. (A) For DSC, samples were heated in an inert nitrogen atmosphere with a nitrogen flow rate of 20 mL/min, in a heating cycle between 25 and 500 °C with a heating rate of 10 °C/min. From bottom to top: DSC thermograms of neat PLLA, PCL, PLGA, and LBL MS composed of all three polymers, with melting peaks at 173, 63.7, and 82.5 °C for neat polymers, respectively, and at 61.4 and 168 °C for LBL MS. (B) TGA thermograms of neat polymers – PLLA, PCL and PLGA, and LBL MS were obtained by heating the samples from 25 °C to 700 °C at a rate of 10 °C/min under nitrogen atmosphere, (C) Differential thermal analysis (DTA) of neat polymers – PLLA, PCL and PLGA, and LBL MS, showing characteristic decomposition peak at 330 and 388 °C, shifted yet closely superimpose with the peaks of the neat polymers, (D) Representative SEM images of LBL MS stored at room temperature, 4 °C, −20 °C, and -80 °C were taken at days 7, 28, 42 and 130, showing no external morphological changes. Scale bar: depicted at the lower bar of respective images.

RNA/DNA delivery applications.[8,65] In comparison to single polymer MS, the core-shell MS are capable of loading multiple payloads. The core-shell MS offer potential sustained and controlled release, timing, and dosing.[33] As mentioned earlier, drug release from MS are dependent on particle size,[59] polymer composition,[60] and the presence/absence of porosity.[61] Thus, to determine the effect of porosity on the release kinetics of the LBL MS, two formulations of porous and non-porous LBL MS encapsulating RhB dye (referred to as LBL-RhB MS) were prepared using the single emulsion solvent evaporation method.

LBL-RhB MS were resuspended in a dynamic dissolution tester containing PBS (with 1 % Tween 80, at pH 7.2 and 5.5) to simulate *in vivo* dynamic sink conditions for release (Fig. 7B). The pH was selected to reflect the potential neutral (tissue) or acidic (intracellular) environments where the MS are likely to reside. We monitored the RhB concentration by measuring the absorbance maximum of RhB (λ_{ex} 560 and λ_{em} 585 nm) across time (26 days). This release data was fitted into 2-step release kinetics model. For both non-porous and porous LBL MS, the RhB dye release showed an initial burst release (steep slope) followed
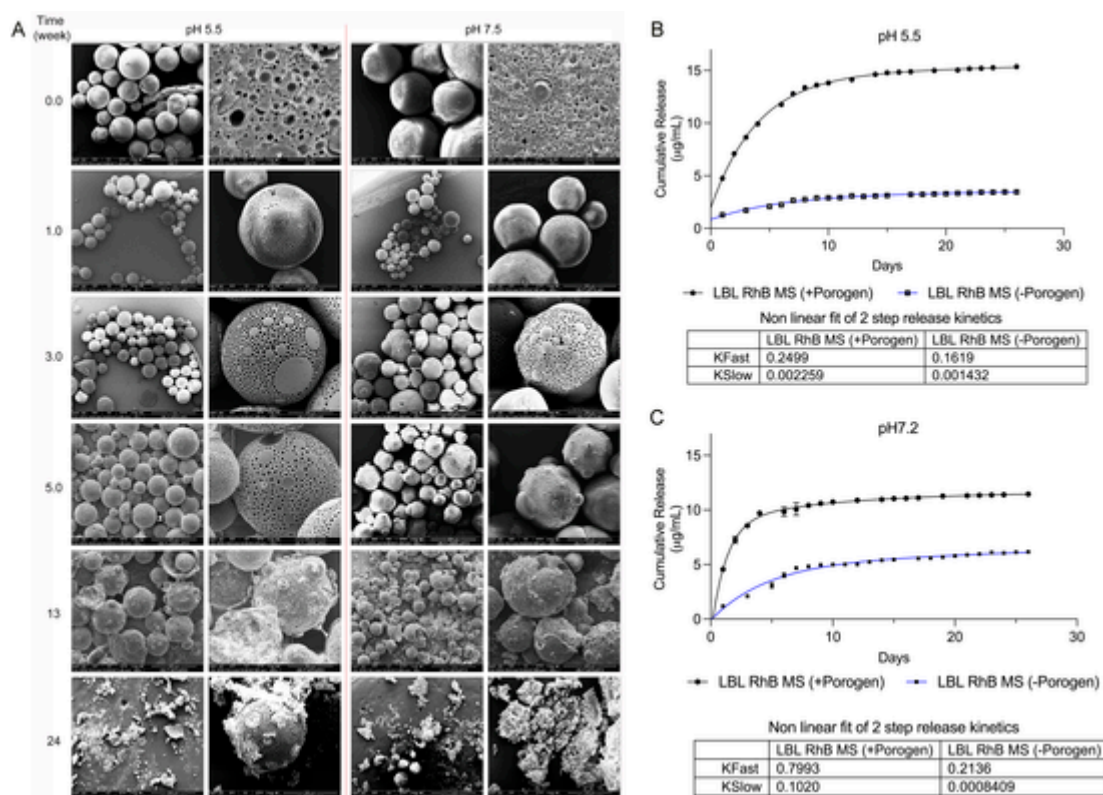
Fig. 7. In vitro simulation of LBL MS biodegradation and release kinetics. (A) LBL MS (200 mg) were immersed in buffered DMEM at pH 5.5 and 7.5. Sink media was replaced with fresh media every seven days, and quantity sufficient LBL MS were collected, washed, freeze-dried and prepared for SEM analysis. The samples were collected over the period of six months to follow the *in vitro* biodegradation process. Scale bar: depicted at lower bar of respective images, (B-C) Non-linear fit of 2-step release kinetics of RhB dye from LBL RhB MS over the period of 26 days at pH 5.5 and 7.2, expressed as µg/mL dye released over time (in days). Elaborations: KFast, fast rate constant; KSlow, slow rate constant; porogen, porous LBL RhB MS; porogen, non-porous LBL-RhB MS.

by a sustained release phase (almost plateau). The initial burst release can be related to the RhB dye adsorbed onto the surface of the MS that would be immediately released during the initial stage. For acidic pH of 5.5 (Fig. 7B), the porous LBL-RhB MS showed faster (K_{Fast} = 0.2499, K_{Slow} = 0.002259, degrees of freedom = 55, R^2 = 0.9972) and greater RhB release than the non-porous LBL-RhB MS (K_{Fast} = 0.1619, K_{Slow} = 0.001432, degrees of freedom = 64, R^2 = 0.9810). The initial burst release was higher for porous LBL-RhB MS, reaching upto 11.77 µg/mL by day 6 as compared to the non-porous LBL-RhB MS reaching only upt o 2.23 µg/mL by day 6, before reaching the sustained release phase. Similarly, for near-neutral pH of 7.2 (Fig. 7C), the porous LBL-RhB MS showed faster (K_{Fast} = 0.7993, K_{Slow} = 0.1020, degrees of freedom = 55, R^2 = 0.9717) and greater RhB release than the non-porous LBL-RhB MS (K_{Fast} = 0.2136, K_{Slow} = 0.0008409, degrees of freedom = 64, R^2 = 0.9679). The initial burst release was also higher for porous LBL-RhB MS, reaching upto 8.56 µg/mL by day 3 as compared to the non-porous LBL-RhB MS reaching only upto 2.09 µg/mL by day 3, before reaching the sustained release phase. Comparing the porous LBL-RhB MS at both pHs, the cumulative amount of dye released were greater for pH 5.5 within comparable time frames.

The higher quantitative release from porous MS at pH 5.5 than pH 7.2 can be attributed to the more significant LBL MS mass loss that occurs due to autocatalysis and pronounced cleavage of ester bonds in polymer chains. This also aligns with the previously reported release kinetics of the positively charged RhB dye in acidic environments.[63,66] Overall, the release data showed that porous MS have faster, and greater cargo release as compared to its non-porous counterparts within the same period. This phenomenon might be explained by differences in surface topography brought about by increased porosity. The higher surface area of the porous LBL MS compared to the non-porous ones

may lead to a faster release rate as porosity and roughness enhance the diffusion of the suspension media into the polymer matrix.[67–69]

Polymer autofluorescence

So far, our data has demonstrated the stable construction of porous LBL MS. Successful demonstration of cargo loading in the MS structure needs affirmation to have true potential in the field of drug delivery. Confirmation of loading is generally investigated either by (i) release study, popular in the case of drug payloads[70,71] where high-performance liquid chromatography is employed for quantification, or (ii) fluorophore-tagged payload for visualization *via* confocal laser scanning microscopy (CLSM).[72,73] To our knowledge, there are no studies clearly stating the acceptable spectral range of excitation and emission wavelengths that can be used for payload-labeling in case of CLSM. Importantly, the data (Fig. 8) demonstrated that the choice of the fluorophore used for labeling needs to account for the polymer type and its autofluorescence. For clarification, the spectral range of excitation and emission wavelengths that were likely to generate sample autofluorescence were tested, which may interfere with the image acquisition of the fluorescently labeled MS payload. All neat polymers and MS produced were excited with one laser, set at either 401, 488, 560, or 639 nm and the emission was measured at 10 nm step separation, between 404 and 660 nm. Based on the mean fluorescent intensity (MFI) measurements of the CLSM images, excitation at 401 nm corresponded to minimal emissions for all samples (Fig. 8 and Fig. S6). The LBL MS, being the combination of all the three polymers, showed comparable MFI measurements to that of PLLA MS (Fig. 8A). Comparing the MFI of the raw polymers (Fig. S6A-C) *versus* respective polymer MS (Fig. 8B-D), it was observed that PCL (raw and MSs) showed similar MFI readings at the different excitation wavelengths (Fig. S6B and 8C). On the

other hand, MFI for raw PLLA (Fig. S6A) and PLGA (Fig. S6C) were higher than its MS counterparts (Fig. 8B and D respectively), when excited at 488, 560, and 639, indicating loss of inherent MFI upon adopting spherical conformation. Moreover, the MFI was observed to be different across polymers (Fig. 8B-D), with PLGA MS showing the least MFI, indicative of the minimal autofluorescence.

Additionally, researchers using PLGA MS do not necessarily have to restrict their choice of the fluorophore to a single wavelength but instead have the options to choose from a broader range, provided the label itself has strong MFI. Overall, for research purposes, fluorophores with excitation wavelengths 401 nm, 488 nm, followed by 639 nm maybe the first, second, and third choices, respectively, considering that the chosen fluorophore-label of the payload itself produces intense signals overriding the effects of any existing autofluorescence. The commonly used excitation and emission in the range of 550–600 nm should not be used for signal tags of interest but can be used as counter autofluorescence for the polymer particles. (See Fig. 9.)

Discussion

Porosity affects the particle's physical properties. These include, but are not limited to, mass density, adsorption,[74] encapsulation, and cargo release[3,4,22] and surface area. Herein we demonstrated that the production, polymer and porogen type and quantity, and its physicochemical properties affect the LBL MS performance properties. While prior works have focused on single MS heterogeneous polymers with variable pore sizes and shapes[75,76] these lead to variabilities in polymer uniformity, scalability and stability. Thus, attaining homogeneity by improving synthesis remained an unmet need.

Each method in producing porous MS[22,28,74,77,78] are limited based on time and expense and requirements for bulk organic solvent volumes, inorganic cations, gases, and supercritical fluids. All affect the degradation of the MS payload. Therefore, a simple and reproducible method of porous MS preparation was needed to create porous particles[22,79] optimized for size, shape, and porosity.[5,18,22,80] To achieve this goal, we tested six porogens that would generate uniform pores in single and multilayered MS that were prepared through conventional solvent evaporation. We produced porous, multilayered MS (LBL MS) by single emulsion solvent evaporation with a unique blend of biodegrad-

able polymers. Food and drug administration (FDA) US approvals and their lack of polymerization led to the choice of PLLA, PLGA, and PCL.

The six porogens were 2-MP, 3-MP, 2-MH, 3-MH, 2,3- 2,3-DMB, and 2,4-DMP and were selected based on their abilities to generate PLLA, PLGA and PCL polymers with varied porosity that included pore size, depth, and density. The mechanism of pore formation also called solvent casting or particulate leaching) are known to affect porogen influx between the inner organic and outer aqueous phase. This occurs in the presence of surfactants and as such can readily generate polymer pores.[22] The mechanisms surrounding porosity differences in the single and multi-polymer MS are subjects of future investigations.

The porogen effect are influenced by the polymer type and monomer composition as well as the process of polymerization. and methods for generation the MS. The particle size, the ratio and volume of the porogen:polymer[81]; and the porogen viscosity-solubility also affect the porogen. In this report we investigated the effects of the porogen polymer ratios and the emulsion and droplet coalescence[82] on the pore-size distribution. The results showed that higher quantities of porogens parallel larger and deeper pores. Interestingly, increasing the porogen quantity also resulted in hemispherical particles. Polymer morphology modulating methodology could influence the physical properties of the porogen and as such play a potential role in industrial and impact resistance plastics coatings,[83] and for drug delivery.[29,84] Further investigations will decipher the relevant kinetic and thermodynamic[85,86] and physicochemical parameters together with the role of hydrocarbon-based reagents in pore formation. of the use of biodegradable polymers[87,88] that can affect interfacial tension and solubility can lead to a better understanding of these systems for drug delivery. and the ultimate goal to improve drug delivery by sustained, controlled rate release at sites of disease or in boosting immune responses through vaccinations. Indeed multilayered MS show lower initial burst release and as such can improve efficiency of immunizations and for sustained drug delivery.[89]

In the current study PCL, PLGA and PLLA created the LBL MS. This demonstrated successful production of double-layered MS, with a shell made of the slow degrading PCL, and a core of fast degrading PLGA. Each were confirmed by microscopy. PCL aided in stability as it demonstrated slow degradation and cargo release rates compared to PLGA and PLLA. The use of three different polymers served to optimize formula-
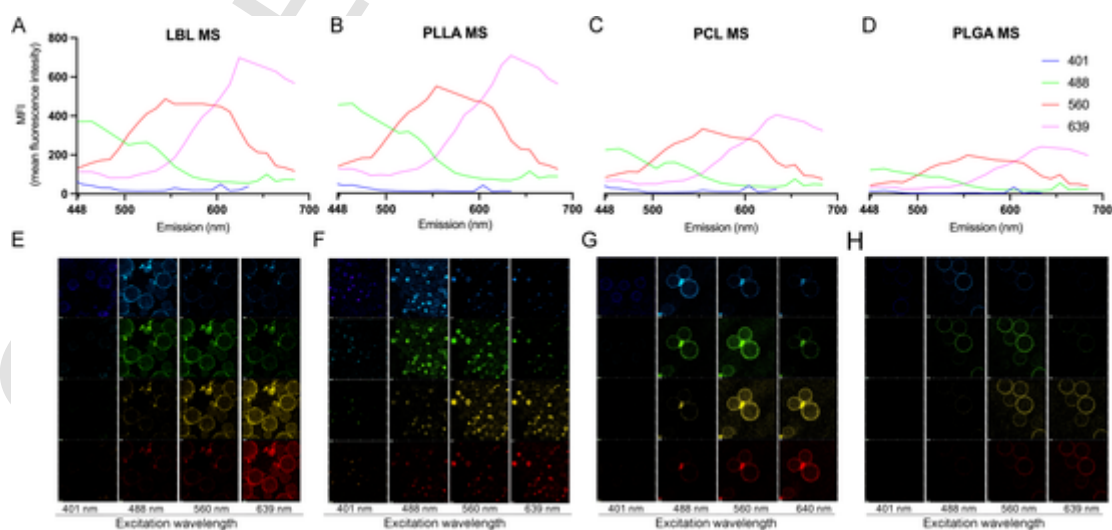

Fig. 8. Autofluorescence emission spectra of individual polymer MS and LBL MS by confocal laser scanning microscopy (CLSM). CLSM spectral analysis was performed for the dry samples of LBL MS (A, E) and individual polymer MS made of PLLA-1 (B, F), PCL (C,F), and PLGA (D,H), under 1a 0× objective. Excitation laser of 401, 488, 560, or 639 nm were used to acquire images at 10 nm step separation of emission wavelengths between 404 and 660 nm. Mean fluorescence intensity (MFI) was measured for the whole panel for each excitation and emission wavelength, using Fiji, and analyzed by GraphPad Prism 9.2. Representative images at emission wavelengths 424, 484, 544, 604 nm (for excitation wavelengths 488, 560, and 639) and at 424, 484, 544, 604 nm (for excitation wavelength 401 nm) are shown.
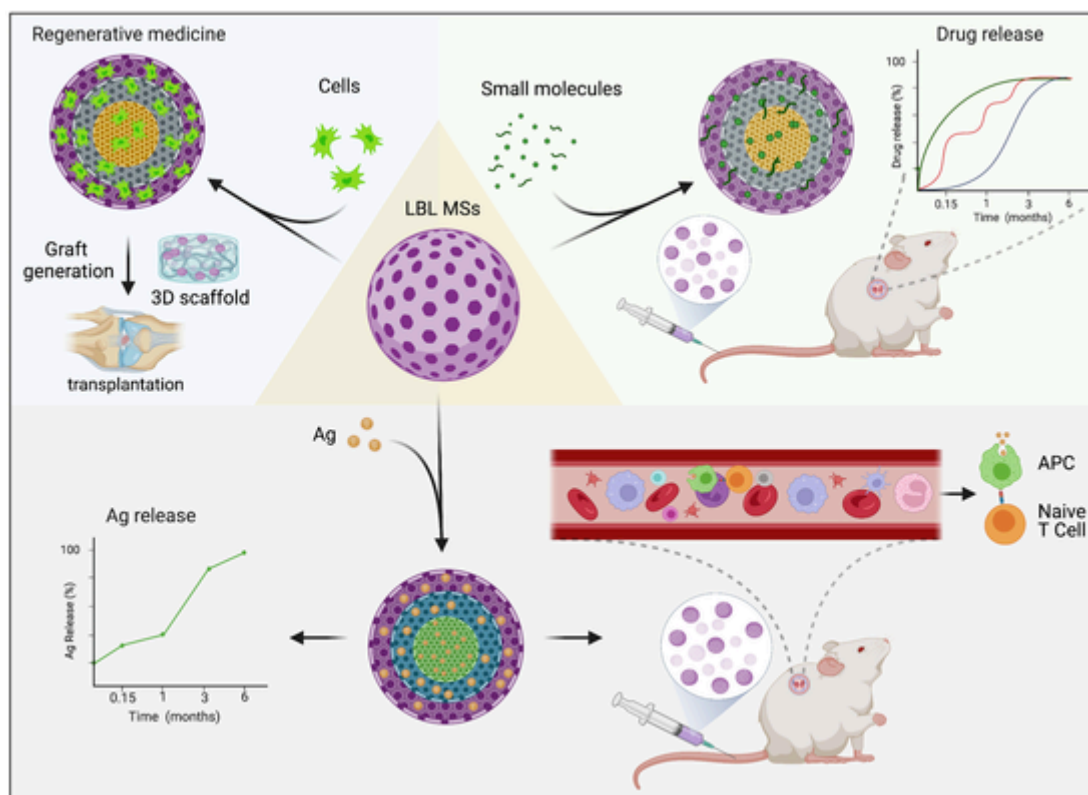
Fig. 9. Potential biomedical applications of porous LBL MS. Representative schematic shows the three potential domains of LBL MS application. First, porous MS are being investigated for better control over the spatial and physical parameters of *in vitro* cell cultures and for predictive screening of therapeutic agents.[101,102] Porous MS can act as substrates or scaffolds with highly interconnected, micrometric pores for cell attachment, infiltration, and tissue model formation. This 3D *in vitro* cell cultures are more representative of *in vivo* conditions than conventional monolayer cultures. Second, porous MS-based drug delivery system offers some advantages over traditional ones, including prolonging the therapeutic effect of drugs, reducing the number of doses, improving patient compliance, and reduce the systemic side effects of drugs.[1,103] At present, there are many studies on the use of biodegradable MS for continuous or targeted drug delivery, involving a wide range of drug types, including anticancer drugs,[95] proteins or peptides,[96] plasmid DNA[97–100] as well as vaccines.[8] Third, polymer MS-based vaccines have been investigated to deliver antigens, as well as co-deliver adjuvants to the same target cell. The targeting and co-delivery functions of polymeric particles are important developments, particularly for diseases that still do not have effective vaccines or require multiple shots to achieve effective immunizations. LBL MS can either serve as sustained (mimicking several small boosters) or pulsatile (mimicking current vaccination strategies) based on antigen release patterns.[8] Abbreviations: Ag; antigen, APC; antigen-presenting cell.

tion density, solvent miscibility, and porogen properties. Based on polymer density and miscibility, PCL and PLGA form separate layers. Based on prior work the external PCL served to protect the encapsulated drugs[90] and highlighting the importance of slow degrading shell architectures. Also, PLLA, a single monomer component of PLGA admixture compensated for the low PLGA porosity. *In toto*, the combination of spectral and thermal data determined the PCL-shell and PLGA-core composition.

We posit that the release of the payload from the LBL MS was controlled through polymer molecular weights, crystallinity, temperature, pH, enzymatic activity, formulation design and porosity rather than polymer degradation.[47,91] Prior works demonstrated the mechanism of polymer degradation ensued by progressive hydrolysis of the its ester bonds,[91–93] followed by heterogenous bulk degradation[47,91] as observed for other LBL MS. Sink condition and bio-secretory fluids, including enzymes serve to catalyze polymer degradation but at a slower rate than the actual payload release. Moreover, depending on the MS payload (for example, drugs, peptides/protein, or antigens), the release kinetics may vary due to differences in the polymer matrix and payload solubility in biological fluids. Release kinetics can be affected by porosity, which can affect the payload diffusion path length and ultimate release.[28] In the most basic sense, MS porosity can promote polymer hydrolysis by increasing surface area and facilitating cargo release by enzymes *in vivo* microenvironment.[94] Future works that will continue

analyses of cargo release over months will provide the exact release kinetics of our LBL MS and demonstrate its role as a sustained carrier.

By virtue of our LBL MS design, the embedded PLLA pellets on the shell component could serve as additional release paradigm. PLLA pellets released over time have the potential to be taken up by tissue phagocytes aka antigen-presenting cells, upon intramuscular administration. This will enhance the mobility and distribution of the PLLA pellets as well as manifesting functional effects at locations apart from the site of injection. Such MS engulfment by cells is expected to expose the MS to intracellular acidic endosomal compartments and follow the degradation pattern shown to occur at lower pH. Moreover, cells would be able to release their cargo elsewhere, highlighting the opportunity for its use as an antigen-carrier to immune cell-populating organs as targets.

For MS applications, loading of the intended cargo, as it will bolster the potential to serve as vehicle for drugs,[95] proteins or peptides,[96] plasmid DNA[97–100] as well as vaccines[8] are essential. As mentioned earlier, a popular method of cargo loading confirmation is through fluorescently labeling it.[72,73] To our knowledge, no reports are available that clearly delineates the acceptable spectral ranges for the fluorescent tags for such a polymer application. Interestingly, it was observed that the raw polymers as well as polymers used in MS form, in either dry from or buffered solution (not shown in this report), had varying intensity of autofluorescence at different excitation wavelengths, which can potentially obscure the actual fluorescent intensity (especially within the

emission range of 540–600 nm) seen from the labeled payload. Therefore, we consider that the limited spectral range of fluorophore labels seen in this report acceptable for payloads.

In conclusion, the current report identified a new class of chemicals, branched aliphatic hydrocarbon-based porogens, to be able to produce uniformly distributed pores on the MS prepared from a single or multipolymer blend. Porous biomaterials have both functional and structural characteristics lending itself to a wide swath of biomedical applications. A methodology for stable MS production was developed, and the production reproducibility demonstrated. Overall, the current study provides an understanding and broadens the reagents and methods optionality for porous MS production, which could be utilized for various biopharmaceutical applications including drug delivery and vaccination. Future investigations into the biological responses of a specific payload would be an appropriate approach for identifying the delivery advantages of LBL MS-based formulations.

Supplementary data to this article can be found online at https://doi.org/10.1016/j.nano.2022.102644.

Ethics committee approval

The experiments performed in this study did not involve any human or animal subjects. Hence, it was exempt from the requirement of UNMC IRB (institutional review board) and UNMC IACUC (institutional animal care and use committee) approvals.

CRediT authorship contribution statement

F.S. devised and planned the experimental approaches; F.S., B.D.K., I.A., Z.Y., M.P., J.D.C., F.I. performed the experiments; B.D.K and H.E.G. conceived the original idea, proof outline and troubleshoots experiments, verified the results, interpreting the results and provided experimental guidance; Z.Y. assisted with Confocal Laser Scanning microscopy and I.A. assisted with confocal Raman microscopy and X-ray microscopic analysis; B.D.K., F.S., M.H., I.A., Z.Y., M.P., M.U.N., M.A., S.M. helped in data analysis and B.D.K., F.S., M.H., M.P., prepared and revised the manuscript including data analysis, figures, tables, and legends; B.D.K. and H.E.G. provided the overall project guidance, supervised the findings of this work, research infrastructure, scientific direction, funding, writing and critical review of the manuscript. All authors read, discussed, and approved the results and contributed to the final version of manuscript.

Declaration of competing interest

F.S., M.P., B.D.K and H.E.G. are named inventors on provisional patents for the new porogens and LBL MS design for SARS-CoV-2 antigen loading as described in this report (63/286,304, 63/158,484). F.S., M.P., B.D.K and H.E.G. hold a patent on 'Microparticle compositions and methods use thereof' (Docket No. 21069PCT, Serial No. PCT/US2022/01950). H.E.G is the co-founder of Exavir Therapeutics.

Data availability

The raw and processed data required to reproduce these findings are available to download from https://data.mendeley.com/datasets/c4yyj74c3p/draft?a=97fb07f8-c622-47fc-aa26-90087753d3f8.

Acknowledgments

References

1. Su Y., Zhang B., Sun R., Liu W., Zhu Q., Zhang X., et al. PLGA-based biodegradable microspheres in drug delivery: recent advances in research and application. *Drug Deliv.* 2021;28:1397–1418.
2. Wang C., Wu D., Yang J., Han H., Xing Z., Zhang Y., et al. Porous PLGA microparticles to encapsulate doxorubicin and polyethylenimine/miR-34a for inhibiting the proliferation and migration of lung cancer. *RSC Adv.* 2015;5: 81445–81448.
3. Kim H., Park H., Lee J., Kim T.H., Lee E.S., Oh K.T., et al. Highly porous large poly(lactic-co-glycolic acid) microspheres adsorbed with palmityl-acylated exendin-4 as a long-acting inhalation system for treating diabetes. *Biomaterials.* 2011;32:1685–1693.
4. Ni R., Muenster U., Zhao J., Zhang L., Becker-Pelster E.M., Rosenbruch M., et al. Exploring polyvinylpyrrolidone in the engineering of large porous PLGA microparticles via single emulsion method with tunable sustained release in the lung: in vitro and in vivo characterization. *J Control Release.* 2017;249:11–22.
5. Saralidze K., Koole L.H., Knetsch M.L.W. Polymeric microspheres for medical applications. *Materials (Basel).* 2010;3:3537–3564.
6. Beck L.R., Pope V.Z., Tice T.R., Gilley R.M. Long-acting injectable microsphere formulation for the parenteral administration of levonorgestrel. *Adv Contracept.* 1985;1:119–129.
7. Zhao Z., Wang Z., Li G., Cai Z., Wu J., Wang L., et al. Injectable microfluidic hydrogel microspheres for cell and drug delivery. *Adv Funct Mater.* 2021;31: 2103339.
8. Lin C.-Y., Lin S.-J., Yang Y.-C., Wang D.-Y., Cheng H.-F., Yeh M.-K. Biodegradable polymeric microsphere-based vaccines and their applications in infectious diseases. *Hum Vaccin Immunother.* 2015;11:650–656.
9. Peyre M., Sesardic D., Merkle H.P., Gander B., Johansen P. An experimental divalent vaccine based on biodegradable microspheres induces protective immunity against tetanus and diphtheria. *J Pharm Sci.* 2003;92:957–966.
10. Yeh M., Chiang C. Inactive vibrio cholerae whole-cell vaccine-loaded biodegradable microparticles: in vitro release and oral vaccination. *J Microencapsul.* 2004;21:91–106.
11. Edwards D.A., Hanes J., Caponetti G., Hrkach J., Ben-Jebria A., Eskew M.L., et al. Large porous particles for pulmonary drug delivery. *Science.* 1997;276: 1868–1871.
12. Malikmmammadov E., Tanir T.E., Kiziltay A., Hasirci V., Hasirci N. PCL and PCL-based materials in biomedical applications. *J Biomater Sci Polym Ed.* 2018;29: 863–893.
13. Woodruff M.A., Hutmacher D.W. The return of a forgotten polymer—polycaprolactone in the 21st century. *Prog Polym Sci.* 2010;35: 1217–1256.
14. Zhang W., Wang X.C., Li X.Y., Zhang L.L., Jiang F. A 3D porous microsphere with multistage structure and component based on bacterial cellulose and collagen for bone tissue engineering. *Carbohydr Polym.* 2020;236:116043.
15. Mittal A., Negi P., Garkhal K., Verma S., Kumar N. Integration of porosity and bio-functionalization to form a 3D scaffold: cell culture studies and in vitro degradation. *Biomed Mater.* 2010;5:045001.
16. Zhang G.-H., Hou R.-X., Zhan D.-X., Cong Y., Cheng Y.-J., Fu J. Fabrication of hollow porous PLGA microspheres for controlled protein release and promotion of cell compatibility. *Chin Chem Lett.* 2013;24:710–714.
17. Sahoo S.K., Panda A.K., Labhasetwar V. Characterization of porous PLGA/PLA microparticles as a scaffold for three dimensional growth of breast cancer cells. *Biomacromolecules.* 2005;6:1132–1139.
18. Dhamecha D., Le D., Movsas R., Gonsalves A., Menon J.U. Porous polymeric microspheres with controllable pore diameters for tissue engineered lung tumor model development. *Front Bioeng Biotechnol.* 2020;8.
19. Vishwa B., Moin A., Gowda D.V., Rizvi S.M.D., Hegazy W.A.H., Abu Lila A.S.,

et al. Pulmonary targeting of inhalable moxifloxacin microspheres for effective management of tuberculosis. *Pharmaceutics*. 2021;13.

20. Cook R.O., Pannu R.K., Kellaway I.W. Novel sustained release microspheres for pulmonary drug delivery. *J Control Release*. 2005;104:79–90.

21. Mendes J.B.E., Riekes M.K., de Oliveira V.M., Michel M.D., Stulzer H.K., Khalil N.M., et al. PHBV/PCL microparticles for controlled release of resveratrol: physicochemical characterization, antioxidant potential, and effect on hemolysis of human erythrocytes. *Sci World J*. 2012;2012:542937.

22. Cai Y., Chen Y., Hong X., Liu Z., Yuan W. Porous microsphere and its applications. *Int J Nanomedicine*. 2013;8:1111–1120.

23. Subia B., Kundu J., Kundu S.C. *Biomaterial scaffold fabrication techniques for potential tissue engineering applications*. 2010.

24. Mansour F.R., Waheed S., Paull B., Maya F. Porogens and porogen selection in the preparation of porous polymer monoliths. *J Sep Sci*. 2020;43:56–69.

25. Freiberg S., Zhu X.X. Polymer microspheres for controlled drug release. *Int J Pharm*. 2004;282:1–18.

26. Kim S.H., Kim J.W., Cho J.C., Weitz D.A. Correction: double-emulsion drops with ultra-thin shells for capsule templates. *Lab Chip*. 2017;17:567.

27. Xia H., Li A., Man J., Li J., Li J. Fabrication of multi-layered microspheres based on phase separation for drug delivery. *Micromachines*. 2021;12:723.

28. Amoyav B., Benny O. Microfluidic based fabrication and characterization of highly porous polymeric microspheres. *Polymers (Basel)*. 2019;11.

29. Su H., Hurd Price C.A., Jing L., Tian Q., Liu J., Qian K. Janus particles: design, preparation, and biomedical applications. *Mater Today Bio*. 2019;4:100033.

30. Go D.P., Palmer J.A., Mitchell G.M., Gras S.L., O'Connor A.J. Porous PLGA microspheres tailored for dual delivery of biomolecules via layer-by-layer assembly. *J Biomed Mater Res A*. 2015;103:1849–1863.

31. Zhang B.J., Han Z.W., Duan K., Mu Y.D., Weng J. Multilayered pore-closed PLGA microsphere delivering OGP and BMP-2 in sequential release patterns for the facilitation of BMSCs osteogenic differentiation. *J Biomed Mater Res A*. 2018;106: 95–105.

32. Toniolo G., Efthimiadou E.K., Kordas G., Chatgilialoglu C. Development of multi-layered and multi-sensitive polymeric nanocontainers for cancer therapy: in vitro evaluation. *Sci. Rep* 2018;8:14704.

33. Xu C., Xu J., Xiao L., Li Z., Xiao Y., Dargusch M., et al. Double-layered microsphere based dual growth factor delivery system for guided bone regeneration. *RSC Adv*. 2018;8:16503–16512.

34. Torchilin V. Multifunctional and stimuli-sensitive pharmaceutical nanocarriers. *Eur J Pharm Biopharm*. 2009;71:431–444.

35. Huang X., Brazel C.S. On the importance and mechanisms of burst release in matrix-controlled drug delivery systems. *J Control Release*. 2001;73:121–136.

36. Koppolu B., Rahimi M., Nattama S., Wadajkar A., Nguyen K.T. Development of multiple-layer polymeric particles for targeted and controlled drug delivery. *Nanomedicine*. 2010;6:355–361.

37. Zhang Y., Wei W., Lv P., Wang L., Ma G. Preparation and evaluation of alginate–chitosan microspheres for oral delivery of insulin. *Eur J Pharm Biopharm*. 2011;77:11–19.

38. Uchida S. Image processing and recognition for biological images. *Dev Growth Differ*. 2013;55:523–549.

39. Otsu N. A threshold selection method from gray-level histograms. *IEEE Trans Syst Man Cybern*. 1979;9:62–66.

40. Singh H. In: Singh H., ed. *Practical Machine Learning and Image Processing: For Facial Recognition, Object Detection, and Pattern Recognition Using Python*. Berkeley, CA: Apress; 2019:63–88.

41. Kornilov A.S., Safonov I.V. An overview of watershed algorithm implementations in open source libraries. *J Imaging*. 2018;4:123.

42. Cobb D.A., Smith N., Deodhar S., Bade A.N., Gautam N., Shetty B.L.D., et al. Transformation of tenofovir into stable ProTide nanocrystals with long-acting pharmacokinetic profiles. *Nat Commun*. 2021;12. 5458- 5458.

43. Kevadiya B.D., Ottemann B., Mukadam I.Z., Castellanos L., Sikora K., Hilaire J.R., et al. Rod-shape theranostic nanoparticles facilitate antiretroviral drug biodistribution and activity in human immunodeficiency virus susceptible cells and tissues. *Theranostics*. 2020;10:630–656.

44. Kevadiya B.D., Joshi G.V., Bajaj H.C. Layered bionanocomposites as carrier for procainamide. *Int J Pharm*. 2010;388:280–286.

45. Mohamed M.H., Wilson L.D. Porous copolymer resins: tuning pore structure and surface area with non reactive porogens. *Nanomaterials*. 2012;2:163–186.

46. Yu B., Xue T., Pang L., Zhang X., Shen Y., Cong H. The effect of different porogens on porous PMMA microspheres by seed swelling polymerization and its application in high-performance liquid chromatography. *Materials (Basel)*. 2018; 11:705.

47. Fu Y., Kao W.J. Drug release kinetics and transport mechanisms of non-degradable and degradable polymeric delivery systems. *Expert Opin Drug Deliv*. 2010;7:429–444.

48. Dorati R., Genta I., Colonna C., Modena T., Pavanetto F., Perugini P., et al. Investigation of the degradation behaviour of poly(ethylene glycol-co-d, l-lactide) copolymer. *Polym Degrad Stab*. 2007;92:1660–1668.

49. Zhang D., Zhao W., Wu Y., Chen Z., Li X. Preparation and properties of multilayer assembled polymer gel microsphere profile control agents. *Polym Eng Sci*. 2019;59:1507–1516.

50. Cheng D., Cao X., Gao H., Ye X., Li W., Wang Y. Engineering PLGA doped PCL microspheres with a layered architecture and an island–sea topography. *RSC Adv*. 2014;4:9031–9038.

51. Kaur T., Kaur R., Kaur A. *Recent biomedical applications and patents on biodegradable polymer*. 2014.

52. Koulouktsi C., Nanaki S., Barmpalexis P., Kostoglou M., Bikiaris D. Preparation

and characterization of alendronate depot microspheres based on novel poly(-ε-caprolactone)/Vitamin E TPGS copolymers. *Int. J. Pharm.X*. 2019;1:100014.

53. Erbetta C.D.Ø.C., Alves R.J., Resende J.M.E., Freitas R.F.D.S., Sousa R.G.D. Synthesis and characterization of poly(D,L-lactide-co-glycolide) copolymer. *J Biomater Nanobiotechnol*. 2012;3(2):18.

54. Benkaddour A., Jradi K., Robert S., Daneault C. Grafting of polycaprolactone on oxidized nanocelluloses by click chemistry. *Nanomaterials (Basel)*. 2013;3: 141–157.

55. Kerber S.J., Barr T.L., Mann G.P., Brantley W.A., Papazoglou E., Mitchell J.C. The complementary nature of x-ray photoelectron spectroscopy and angle-resolved x-ray diffraction part I: background and theory. *J Mater Eng Perform*. 1998;7: 329–333.

56. Kim T., Lee S., Park S.-Y., Chung I. Biodegradable PCL-b-PLA microspheres with nanopores prepared via RAFT polymerization and UV photodegradation of poly(methyl vinyl ketone) blocks. *Polymers*. 2021;13:3964.

57. Ayyoob M., Kim Y.J. Effect of chemical composition variant and oxygen plasma treatments on the wettability of PLGA thin films, synthesized by direct copolycondensation. *Polymers*. 2018;10:1132.

58. Palermo P.J. In: Ahuja S., Scypinski S., eds. *Separation Science and Technology*. Academic Press; 2001:235–267.

59. Berkland C., Kim K., Pack D.W. PLG microsphere size controls drug release rate through several competing factors. *Pharm Res*. 2003;20:1055–1062.

60. Zhang Y., Shams T., Harker A.H., Parhizkar M., Edirisinghe M. Effect of copolymer composition on particle morphology and release behavior in vitro using progesterone. *Mater Des*. 2018;159:57–67.

61. Huang W., Tsui C.P., Tang C.Y., Gu L. Effects of compositional tailoring on drug delivery behaviours of silica xerogel/polymer core-shell composite nanoparticles. *Sci Rep*. 2018;8:13002.

62. Mikolaszek B., Kazlauske J., Larsson A., Sznitowska M. Controlled drug release by the pore structure in polydimethylsiloxane transdermal patches. *Polymers*. 2020; 12:1520.

63. Betancourt T., Shah K., Brannon-Peppas L. Rhodamine-loaded poly(lactic-co-glycolic acid) nanoparticles for investigation of in vitro interactions with breast cancer cells. *J Mater Sci Mater Med*. 2009;20:387–395.

64. Siepmann J., Elkharraz K., Siepmann F., Klose D. How autocatalysis accelerates drug release from PLGA-based microparticles: a quantitative treatment. *Biomacromolecules*. 2005;6:2312–2319.

65. Sharma N., Purwar N., Gupta P. Microspheres as drug carriers for controlled drug delivery: a review. *Int J Pharm Sci Res*. 2015;6:4579–4587.

66. Pramanik S.K., Seneca S., Peters M., D'Olieslaeger L., Reekmans G., Vanderzande D., et al. Morphology-dependent pH-responsive release of hydrophilic payloads using biodegradable nanocarriers. *RSC Adv*. 2018;8: 36869–36878.

67. Amoyav B., Benny O. Microfluidic based fabrication and characterization of highly porous polymeric microspheres. *Polymers*. 2019;11:419.

68. Klose D., Siepmann F., Elkharraz K., Krenzlin S., Siepmann J. How porosity and size affect the drug release mechanisms from PLGA-based microparticles. *Int J Pharm*. 2006;314:198–206.

69. Chew S.A., Arriaga M.A., Hinojosa V.A. Effects of surface area to volume ratio of PLGA scaffolds with different architectures on scaffold degradation characteristics and drug release kinetics. *J Biomed Mater Res A*. 2016;104: 1202–1211.

70. Jiang C., Kuang L., Merkel M., Yue F., Cano-Vega M., Narayanan N., et al. Biodegradable polymeric microsphere-based drug delivery for inductive browning of fat. *Front Endocrinol*. 2015;6.

71. Kim Y., Park E.J., Kim T.W., Na D.H. Recent progress in drug release testing methods of biopolymeric particulate system. *Pharmaceutics*. 2021;13.

72. Liu Z., Ye W., Zheng J., Wang Q., Ma G., Liu H., et al. Hierarchically electrospraying a PLGA@chitosan sphere-in-sphere composite microsphere for multi-drug-controlled release. *Regen Biomater*. 2020;7:381–390.

73. Li J., Yang L., Zhu C., Peng T., Huang D., Ma X., et al. Release mechanisms of bovine serum albumin loaded–PLGA microspheres prepared by ultra-fine particle processing system. *Drug Deliv Transl Res*. 2020;10:1267–1277.

74. Ghosh Dastidar D., Saha S., Chowdhury M. Porous microspheres: Synthesis, characterisation and applications in pharmaceutical & medical fields. *Int J Pharm*. 2018;548:34–48.

75. Maciejewska M., Gawdzik B., Rogulska M. Regular polymeric microspheres with highly developed internal structure and remarkable thermal stability. *Materials (Basel)*. 2021;14.

76. Chen Q., Shi T., Han F., Li Z., Lin C., Zhao P. Porous polystyrene monoliths and microparticles prepared from core cross-linked star (CCS) polymers-stabilized emulsions. *Sci Rep*. 2017;8:8493.

77. Kim D.H., Jeong J.H., Woo H.-C., Kim M.H. Synthesis of highly porous polymer microspheres with interconnected open pores for catalytic microreactors. *Chem Eng J*. 2021;420:127628.

78. Park J.-H., Han C.-M., Lee E.-J., Kim H.-W. Preparation of highly monodispersed porous-channeled poly(caprolactone) microspheres by a microfluidic system. *Mater Lett*. 2016;181:92–98.

79. Gao Y., Bai Y., Zhao D., Chang M.-W., Ahmad Z., Li J.-S. Tuning microparticle porosity during single needle electrospraying synthesis via a non-solvent-based physicochemical approach. *Polymers*. 2015;7:2701–2710.

80. Laeschke K. Biocompatibility of microparticles into soft tissue fillers. *Semin Cutan Med Surg*. 2004;23:214–217.

81. Mohamed M.H., Wilson L.D. Porous copolymer resins: tuning pore structure and surface area with non reactive porogens. *Nanomaterials (Basel)*. 2012;2:163–186.

82. Hao D.-X., Gong F.-L., Wei W., Hu G.-H., Ma G.-H., Su Z.-G. Porogen effects in

synthesis of uniform micrometer-sized poly(divinylbenzene) microspheres with high surface areas. *J Colloid Interface Sci*. 2008;323:52–59.

83. Yamashita N., Konishi N., Tanaka T., Okubo M. Preparation of hemispherical polymer particles by cleavage of a Janus poly(methyl methacrylate) /polystyrene composite particle†Part CCCLVII of the series "studies on suspension and emulsion". *Langmuir*. 2012;28:12886–12892.

84. Matsumoto A., Watanabe C., Murakami M. Janus microspheres for enhanced enteral drug delivery: preparation and orientated attachment to a Caco-2 monolayer. *Drug Discov Ther*. 2019;13:343–353.

85. González-Ortiz L.J., Asua J.M. Development of particle morphology in emulsion polymerization. 2 Cluster dynamics in reacting systems. *Macromolecules*. 1996;29: 383–389.

86. Durant Y.G., Carrier R., Sundberg D.C. Mathematical model for the emulsion polymerization reaction kinetics of two phase latex particles. *Polym React Eng*. 2003;11:433–455.

87. Milosevic M., Stojanovic D.B., Simic V., Grkovic M., Bjelovic M., Uskokovic P.S., et al. Preparation and modeling of three-layered PCL/PLGA/PCL fibrous scaffolds for prolonged drug release. *Sci Rep*. 2020;10:11126.

88. Zeng J., Xu X., Chen X., Liang Q., Bian X., Yang L., et al. Biodegradable electrospun fibers for drug delivery. *J Control Release*. 2003;92:227–231.

89. Ko J.T., Jung H.J., Mo J.H., Cho J.S., Yuk S.H., Shin H.S., et al. The double-layered microsphere: encapsulation of water-soluble protein with PLGA. *Key Eng Mater*. 2007;342–343:513–516.

90. Kim G., Yoon H., Park Y. Drug release from various thicknesses of layered mats consisting of electrospun polycaprolactone and polyethylene oxide micro/nanofibers. *Appl Phys A*. 2010;100:1197–1204.

91. Bartnikowski M., Dargaville T.R., Ivanovski S., Hutmacher D.W. Degradation mechanisms of polycaprolactone in the context of chemistry, geometry and environment. *Prog Polym Sci*. 2019;96:1–20.

92. Zolnik B.S., Burgess D.J. Effect of acidic pH on PLGA microsphere degradation and release. *J Control Release*. 2007;122:338–344.

93. Netti P.A., Biondi M., Frigione M. Experimental studies and modeling of the degradation process of poly(lactic-co-glycolic acid) microspheres for sustained protein release. *Polymers (Basel)*. 2020;12.

94. Thananukul K., Kaewsaneha C., Opaprakasit P., Lebaz N., Errachid A., Elaissari A. Smart gating porous particles as new carriers for drug delivery. *Adv Drug Deliv Rev*. 2021;174:425–446.

95. Ni G., Yang G., He Y., Li X., Du T., Xu L., et al. Uniformly sized hollow microspheres loaded with polydopamine nanoparticles and doxorubicin for local chemo-photothermal combination therapy. *Chem Eng J*. 2020;379:122317.

96. Zhai P., Chen X.B., Schreyer D.J. PLGA/alginate composite microspheres for hydrophilic protein delivery. *Mater Sci Eng C Mater Biol Appl*. 2015;56:251–259.

97. Herrmann V.L., Hartmayer C., Planz O., Groettrup M. Cytotoxic T cell vaccination with PLGA microspheres interferes with influenza A virus replication in the lung and suppresses the infectious disease. *J Control Release*. 2015;216: 121–131.

98. Lu Y., Wu F., Duan W., Mu X., Fang S., Lu N., et al. Engineering a "PEG-g-PEI/DNA nanoparticle-in- PLGA microsphere" hybrid controlled release system to enhance immunogenicity of DNA vaccine. *Mater Sci Eng C Mater Biol Appl*. 2020; 106:110294.

99. Jang J.-H., Shea L.D. Intramuscular delivery of DNA releasing microspheres: microsphere properties and transgene expression. *J Control Release*. 2006;112: 120–128.

100. Parsa S., Wang Y., Fuller J., Langer R., Pfeifer B.A. A comparison between polymeric microsphere and bacterial vectors for macrophage P388D1 gene delivery. *Pharm Res*. 2008;25:1202–1208.

101. Tan Y.J., Tan X., Yeong W.Y., Tor S.B. Hybrid microscaffold-based 3D bioprinting of multi-cellular constructs with high compressive strength: a new biofabrication strategy. *Sci Rep*. 2016;6:39140.

102. Su X., Tan M., Duan B., Cai J., Jiang W., Zhang L. Hierarchical microspheres with macropores fabricated from chitin as 3D cell culture. *J Mater Chem B*. 2019;7: 5190–5198.

103. Ozeki T., Kaneko D., Hashizawa K., Imai Y., Tagami T., Okada H. Improvement of survival in C6 rat glioma model by a sustained drug release from localized PLGA microspheres in a thermoreversible hydrogel. *Int J Pharm*. 2012; 427:299–304.